

Inversion for Inferring Solar Meridional Circulation: The Case with Constraints on Angular Momentum Transport inside the Sun

YOSHIKI HATTA,^{1,2} HIDEYUKI HOTTA,¹ AND TAKASHI SEKII^{2,3}

¹*Institute for Space-Earth Environmental Research, Nagoya University
Furo-cho, Chikusa-ku, Nagoya, Aichi 464-8601, Japan*

²*National Astronomical Observatory of Japan
2-21-1 Osawa, Mitaka, Tokyo 181-8588, Japan*

³*Astronomical Science Program, The Graduate University for Advanced Studies, SOKENDAI
2-21-1 Osawa, Mitaka, Tokyo 181-8588, Japan*

ABSTRACT

We have carried out inversions of travel times as measured by Gizon et al. (2020) to infer the internal profile of the solar meridional circulation (MC). A linear inverse problem has been solved by the regularized least-squares method with a constraint that the angular momentum (AM) transport by MC should be equatorward (HK21-type constraint). Our motivation for using this constraint is based on the result by Hotta & Kusano (2021) where the solar equator-fast rotation was reproduced successfully without any manipulation. The inversion result indicates that the MC profile is a double-cell structure if the so-called HK21 regime, in which AM transported by MC sustains the equator-fast rotation, correctly describes the physics inside the solar convective zone. The sum of the squared residuals computed with the inferred double-cell MC profile is comparable to that computed with the single-cell MC profile obtained when we exclude the HK21-type constraint, showing that both profiles can explain the data more or less at the same level. However, we also find that adding the HK21-type constraint degrades the resolution of the averaging kernels. Although it is difficult for us to determine the large-scale morphology of the solar MC at the moment, our attempt highlights the relevance of investigating the solar MC profile from both theoretical and observational perspectives.

Keywords: Solar interior(1500) — Solar convective zone(1998) — Solar meridional circulation(1874)
— Helioseismology(709)

1. INTRODUCTION

The meridional circulation (MC) is one component of the Sun's large-scale flows. On the surface of the Sun, the velocity amplitude of the solar MC is small ($\sim 10 - 20 \text{ m s}^{-1}$; e.g. Hathaway 1996; Rightmire-Upton et al. 2012) compared with the other velocity components, such as granulation ($\sim 10^3 \text{ m s}^{-1}$; e.g. Nordlund et al. 2009) and rotation ($\sim 2 \times 10^3 \text{ m s}^{-1}$; e.g. Thompson et al. 1996; Howe 2009). However, it nevertheless has substantial impacts on magnetic flux transport toward the pole (Wang et al. 1989); thus, it possibly controls the periodicity of the solar activity cycle (e.g. Charbonneau 2020). In addition, the solar MC redistributes the an-

gular momentum (AM) inside the convective zone (e.g. Miesch 2005). In a statistically steady state, the AM profile is determined by a balance between the amount of AM transported by MC and that transported by turbulent Reynolds stresses (c.f. gyroscopic pumping, Miesch & Hindman 2011). Therefore, we can extract information about the turbulent stresses in the convective zone once we know the internal MC profile because we already have quite a good picture of the AM profile in the solar convective zone as shown by global helioseismology (e.g. Schou et al. 1998). As such, it is of great importance to investigate the solar internal MC profile to improve our understanding of the solar dynamo mechanism.

One of the most powerful methods for inferring the solar internal MC profile is time-distance helioseismology (Duvall et al. 1993; Gizon et al. 2010) in which wave travel times between two points on the solar surface

may be linearly related to internal flow fields via forward modeling formulated based on, for example, ray approximation (e.g. Kosovichev & Duvall 1997) or Born approximation (e.g. Gizon & Birch 2002). The measured wave travel times are then inverted to estimate the flow fields.

Because of the relevance of the MC in the solar dynamo, there have been multiple attempts to infer the internal MC profile via time–distance helioseismology (Giles et al. 1997; Giles 2000; Zhao & Kosovichev 2004; Chou & Ladenkov 2005; Zhao et al. 2013; Jackiewicz et al. 2015; Rajaguru & Antia 2015; Chen & Zhao 2017; Gizon et al. 2020; Herczeg & Jackiewicz 2023). We have seen good agreement for the MC profile in the subsurface region ($r/R_{\odot} > 0.95$ where r and R_{\odot} are the distance from the solar center and solar radius, respectively), as the poleward flow persists in the subsurface region with a peak velocity amplitude of about $\sim 10 - 20 \text{ m s}^{-1}$. In contrast, there has been no consensus for deeper regions (see Hanasoge 2022; Hotta et al. 2023). It is not clear whether the MC throughout the convective zone is a single- or multiple-cell structure (e.g. Gizon et al. 2020; Herczeg & Jackiewicz 2023). The difference should be critical for the periodicity of the solar activity cycle as indicated by flux-transport dynamo models (e.g. Choudhuri et al. 1995; Dikpati & Charbonneau 1999). It has been also recently pointed out by Bekki et al. (2024) that a single-cell MC profile and tiny negative superadiabaticity around the lower convective boundary can produce the latitudinal entropy gradient which is consistent with observed properties of the solar inertial modes (Gizon et al. 2021).

A primary reason for the difficulty in estimating the internal MC profile in the deep convective zone is that the MC velocity amplitude is expected to be so small there (\sim a few m s^{-1} ; Giles 2000) that the travel time perturbations caused by MC ($\sim 0.1 \text{ s}$) are small and comparable to the observational uncertainties that are dominated by realization noises (Braun & Birch 2008; Stejko et al. 2021). Inversion results are thus quite sensitive to the noise in the travel time perturbations. Although we can somehow obtain solutions by imposing constraints or regularization in inversion procedures, there is no unique method for imposing constraints (or how we add prior information), resulting in a number of possible solutions.

Given the current level of the low signal-to-noise ratio (that can be possibly increased by some future solar polar missions; Featherstone et al. 2023) as well as the difficulty in MC inversion, improving on the inversion procedures is certainly valuable. For example, Herczeg & Jackiewicz (2023) applied Bayesian statistics to carry

out MC inversion, which has enabled them to partly avoid the arbitrary choice of some regularization terms. Such attempts to reconsider inversion procedures from various perspectives will be helpful for analyzing the data introduced by future observations.

In this paper, we focus on the inversion procedure. Specifically, we carry out MC inversion by imposing constraints inspired by the results from numerical simulations of solar convection in addition to those adopted conventionally, such as the mass conservation constraint.

There are currently two main results widely accepted that successfully reproduce the solar differential rotation where the equator rotates faster than the pole (i.e., equator-fast rotation). In one regime, rotation has significant impacts on turbulent convection, and the resultant AM transport by Reynolds stress is crucial for achieving equator-fast rotation (e.g. Gastine et al. 2014; Featherstone & Miesch 2015; Karak et al. 2015; Käpylä 2023), called the RS regime in this work. However, it should be noted that we cannot realize the RS regime without adopting strong effective diffusion and viscosity that do not seem to be compatible with realistic solar parameters.

Another regime is the so-called HK21 regime that has been proposed by Hotta & Kusano (2021) who reproduce the solar equator-fast rotation without any manipulation. In the HK21 regime, the magnetic field plays an important role in AM redistribution, and the equator-fast rotation is sustained by the equatorward AM transport by MC (Hotta & Kusano 2021; Hotta et al. 2022). Because the AM transport by MC is directly related to the meridional flow field, the suggested equatorward AM transport by MC can be used as a physically motivated constraint for the MC profile if the physics found in the HK21 regime is assumed to be correct. Therefore, as a first step toward implementing physics constraints on MC inversion, we would like to infer the large-scale morphology of the solar MC profile with the constraint on AM transport by MC.

This paper is structured as follows. In Section 2, we explain the data used in MC inversion. We then present how we invert the travel times to infer the MC profile (Section 3) where we introduce constraints devised based on the numerical results found in the HK21 regime (hereafter the HK21-type constraint). The results for MC inversion that are obtained with or without the HK21-type constraint are shown in Section 4. Although the main focus of this paper is on inversion with a constraint on AM transport by MC, we also carry out inversion with a constraint appropriate for the RS regime (hereafter the RS-type constraint) in a rather crude manner. We dis-

cuss all the inversion results obtained in this study in Section 5. We conclude in Section 6.

2. DATA AND KERNELS

To carry out MC inversion, we used the travel times, variance–covariance matrix, and sensitivity kernels, which are all publicly available from Gizon et al. (2020); Gizon et al. (2020) (Open Research Data Repository of the Max Planck Society). We give a brief summary of the data in the following few paragraphs (see Gizon et al. 2020, hereafter G20).

We first explain how the travel times are computed in G20. In general, the starting point for measuring travel times is an observation of the surface velocity fields of the Sun. G20 used two series of Dopplergrams, namely, the one obtained by the Solar and Heliospheric Observatory (SOHO)/Michelson Doppler Imager (MDI) (Scherer et al. 1995) for cycle 23 (duration ~ 11 years) and the other obtained by the Global Oscillation Network Group (GONG) (Hill et al. 1996) for cycle 24 (duration ~ 11 years).

After substantial data reduction efforts to render the raw Dopplergrams suitably for time–distance helioseismic analyses (see Liang et al. 2017, 2018), cross-correlation functions of the velocity fields for multiple pairs of points on the solar surface are computed. These point pairs aligned in the north–south direction were chosen to measure travel times that are sensitive to MC. Spatial averaging of the cross-correlation functions has been conducted to reduce the realization noise in travel time measurements. This spatial averaging has been characterized by two parameters, namely, λ , the latitude of the center of the circle whose northern and southern arcs are used for spatial averaging, and Δ , the angular distance between the two opposing arcs. The details for the data reduction, arc geometry, and how the spatial averaging has been done can be found in Liang et al. (2017, 2018).

Then, with the cross-correlation functions averaged spatially, G20 applied a one-parameter fitting method to compute the north–south travel times (Gizon & Birch 2002, 2004). The computed travel times are given as a function of λ and Δ that were introduced in the previous paragraph. The parameter ranges are $-54^\circ < \lambda < 54^\circ$, where the positive (negative) value represents the northern (southern) hemisphere, and $6^\circ < \Delta < 42^\circ$ (in units of degrees in both cases). The total number of travel times thus computed is $N_d = 9120$ for each of the MDI and GONG data. The variance–covariance of the travel times is also evaluated by G20 (see also Gizon & Birch 2004; Fournier et al. 2014).

We then introduce a series of equations to infer the internal MC profile with the measured travel times. First, the forward problem must be solved (Gizon & Birch 2002). G20 relied on the Born approximation, which could be used to relate the i -th component of the north–south travel times τ_i to the meridional flow field as:

$$\tau_i = \iint (\mathcal{K}_i^r(r, \theta)U_r(r, \theta) + \mathcal{K}_i^\theta(r, \theta)U_\theta(r, \theta))drd\theta \quad (1)$$

$$(i = 1, \dots, N_d; N_d = 9120),$$

where θ is the colatitude. The radial and latitudinal components of the meridional flow field are denoted by U_r and U_θ . The corresponding sensitivity kernels are \mathcal{K}_i^r (\mathcal{K}_i^θ) that have been calculated by numerically solving wave propagation in a particular solar model (Gizon et al. 2017). Axisymmetry is assumed to derive the presented equation (Fournier et al. 2018). Index i designates a certain pair (λ, Δ) , namely, i runs from 1 to N_d in the case of G20’s data. The integration is conducted over the whole solar interior (although the meridional flow velocity is assumed to be zero outside the convective zone, as mentioned in Section 3.1.)

To parameterize the meridional flow field, G20 expanded it in both the radial and latitudinal directions with the cubic B-spline functions $Q_k(r)$ ($k = 1, \dots, N_k$; $N_k = 20$) and Legendre polynomials $P_l(\cos \theta)$ ($l = 0, \dots, N_l - 1$; $N_l = 16$), respectively. The 18 knots used for defining the B-spline function are uniformly spaced between the bottom of the convective zone and the solar surface. The explicit expression of the expanded meridional flow field is then

$$U_s(r, \theta) = \sum_{j=(k,l)} u_{s,j}Q_k(r)P_l(\cos \theta) \quad (2)$$

$$(s = r \text{ or } \theta)$$

$$(k = 1, \dots, N_k; N_k = 20)$$

$$(l = 0, \dots, N_l - 1; N_l = 16),$$

in which index s represents r or θ . A certain pair (k, l) is represented by the index j that runs from 1 to N_j where $N_j = N_k \times N_l$. The expansion coefficient is denoted by $u_{s,j}$. By defining an N_j -dimensional vector \mathbf{u}_r (\mathbf{u}_θ) whose j -th element is $u_{r,j}$ ($u_{\theta,j}$), Equation (1) can be rewritten in matrix form:

$$\boldsymbol{\tau} = K\mathbf{u} + \mathbf{e}, \quad (3)$$

where \mathbf{u} is a $2N_j$ -dimensional vector defined as:

$$\mathbf{u} = \begin{pmatrix} \mathbf{u}_r \\ \mathbf{u}_\theta \end{pmatrix}. \quad (4)$$

The N_d -dimensional vector $\boldsymbol{\tau}$ represents the measured travel times. Note that the N_d -dimensional vector \mathbf{e} is added in the expression as an observational error. The statistical property of \mathbf{e} is described by the $N_d \times N_d$ variance–covariance matrix (E) of the travel time. In Equation (3), the sensitivity kernel is represented by the $N_d \times 2N_j$ matrix K consisting of two $N_d \times N_j$ matrices K^r and K^θ that are defined as

$$(K^s)_{ij} = \iint \mathcal{K}_i^s(r, \theta) Q_k(r) P_l(\cos \theta) dr d\theta, \quad (5)$$

with which $K = (K^r \ K^\theta)$. The index s again denotes r or θ . Note that $j = (k, l)$.

The measured travel times, variance–covariance matrix, basis functions, and expanded kernels are provided by G20. Using the data described in this section, the matrix equation (3) is to be inverted with some regularization and constraints on the MC profile, as shown in Section 3.

3. METHOD

In this section, we explain how to invert Equation (3). Basically, the regularized least-squares (RLS) method is used, thus, we first briefly review the RLS method in Section 3.1. We then present a constraint on MC inversion that is devised based on the result of Hotta & Kusano (2021) (hereafter HK21) (see Section 1) in Section 3.2. Because we have free parameters in the inversion procedure, which are called trade-off parameters, the process for determining these parameters is given in Section 3.3.

3.1. The regularized least-squares method

It is often the case that the least-squares solution of Equation (3) is unstable against observational uncertainties and/or numerical errors; therefore, the inverse problem is ill-posed. However, an ill-posed problem can be turned into a well-posed one by adding prior information such as that the solution should be flat or smooth enough to exhibit no discontinuous features which are difficult to accept from the physics point of view. This procedure is called regularization.

In the RLS method (Tikhonov & Arsenin 1977), what we minimize is:

$$X = |E^{-1/2}(\boldsymbol{\tau} - K\mathbf{u})|^2 + \alpha |D\mathbf{u}|^2, \quad (6)$$

where the first term on the right-hand side represents the sum of squared residuals between the observation ($\boldsymbol{\tau}$) and model ($K\mathbf{u}$) normalized by the variance–covariance matrix (E). The second term represents the regularization term. For example, if the matrix D is a first-(second-)derivative operator, the term $D\mathbf{u}$ represents

the flatness (smoothness) of the flow field (e.g. Rajaguru & Antia 2015). In this study, we follow G20 and define an $N_D \times 2N_j$ matrix D (where N_D is the number of mesh points in the (r, θ) -plane) so that $D\mathbf{u}$ represents the weighted vorticity of the MC flow field (see the supplementary material of G20, or Appendix C of this paper for more details). The balance between the first and second terms in Equation (6) depends on the trade-off parameter α . We obtain the least-squares solution in the limit $\alpha \rightarrow 0$. Conversely, the solution is determined by the prior information alone when $\alpha \rightarrow \infty$. For a particular value of α , we can obtain the corresponding RLS solution that minimizes the quantity X . Note that there is no established way of choosing a single most appropriate value of α . We discuss the point in Section 3.3.

Besides regularization, we consider two additional constraints on the meridional flow field that are conventionally adopted in some previous studies (e.g. Rajaguru & Antia 2015; Gizon et al. 2020; Herczeg & Jackiewicz 2023). One is the mass conservation $\nabla \cdot (\rho\mathbf{U}) = 0$ where $\mathbf{U} = (U_r, U_\theta)^T$, and the other one is given based on the assumption that MC is confined in the solar convective zone and does not cross the convective boundary. Both constraints can be expressed as linear constraints (in terms of the expansion coefficients \mathbf{u}) as follows:

$$C\mathbf{u} = \mathbf{0} \quad (7)$$

for the former, and

$$S\mathbf{u} = \mathbf{0} \quad (8)$$

for the latter. The detailed derivation of the matrices C and S is found in the supplementary material in G20. We have used C and S that are provided by G20. It should be noted that these two constraints are strict in a sense that Equations (7) and (8) should always be satisfied.

Then, what we must minimize with the strict constraints is:

$$X' = |E^{-1/2}(\boldsymbol{\tau} - K\mathbf{u})|^2 + \alpha |D\mathbf{u}|^2 + \boldsymbol{\kappa} \cdot C\mathbf{u} + \boldsymbol{\mu} \cdot S\mathbf{u}, \quad (9)$$

where we have two additional terms (see Equation (6)) with Lagrange multipliers $\boldsymbol{\kappa}$ and $\boldsymbol{\mu}$. Minimization of the quantity X' is achieved by the vectors \mathbf{u} , $\boldsymbol{\kappa}$, and $\boldsymbol{\mu}$ that satisfy the following matrix equation:

$$\begin{pmatrix} A & C^T & S^T \\ C & O & O \\ S & O & O \end{pmatrix} \begin{pmatrix} \mathbf{u} \\ \boldsymbol{\kappa} \\ \boldsymbol{\mu} \end{pmatrix} = \begin{pmatrix} K^T E^{-1} \boldsymbol{\tau} \\ \mathbf{0} \\ \mathbf{0} \end{pmatrix}, \quad (10)$$

where we have introduced a $2N_j \times 2N_j$ submatrix A that is defined as:

$$A = K^T E^{-1} K + \alpha D^T D. \quad (11)$$

This equation is derived by equating the gradient of X' to $\mathbf{0}$. Let us denote by $\hat{\mathbf{u}}_{\text{RLS}}$ the RLS solution of Equation (3) obtained with the constraints (7) and (8).

Before concluding this section, we would like to mention that without any other constraints, we have obtained the RLS solution $\hat{\mathbf{u}}_{\text{RLS}}$ that exhibits the single-cell MC profile; hence, we have confirmed the same result as that found by G20. We discuss whether this result changes or not later in Section 4 when we further add the HK21-type constraint.

3.2. Constraint on the MC profile devised based on numerical results found in the HK21 regime (the HK21-type constraint)

In this section, we present how to impose the HK21-type constraint on Equation (3). As mentioned in Section 1, the magnetic field plays a significant role in AM transport in this regime, and the equator-fast rotation is sustained by the AM transported by the MC flow (Hotta et al. 2022). This can be confirmed by looking at the latitudinal AM flux by MC that is defined as:

$$F_{\text{MC},\theta} = \rho \mathcal{L} U_\theta, \quad (12)$$

in which the density and specific AM are denoted by ρ and \mathcal{L} , respectively. Note that $\mathcal{L} = r \sin \theta v_\phi$ where v_ϕ represents the rotational velocity (as a function of r and θ) in the inertial frame. Figure 1 shows the latitudinal AM flux by MC radially averaged (hereafter $\bar{F}_{\text{MC},\theta}(\theta)$) that has been computed with the result of numerical simulation by HK21, highlighting the fact that the MC transports the AM toward the equatorial region in the HK21 regime. See Equation (C22) for the definition of $\bar{F}_{\text{MC},\theta}(\theta)$.

Because the latitudinal AM flux ($F_{\text{MC},\theta}$) is proportional to the latitudinal component of the meridional flow field (U_θ), we can readily obtain a linear constraint for the meridional flow field. In this study, we first assume that the latitudinal average of $\bar{F}_{\text{MC},\theta}(\theta)$ is positive (negative) in the northern (southern) hemisphere to reproduce the net AM transport by MC toward the equator (Figure 1). The assumption can be expressed as:

$$D_{\text{HK1}} \mathbf{u} = \mathbf{b}, \quad (13)$$

where D_{HK1} is a $2 \times 2N_j$ matrix with which $D_{\text{HK1}} \mathbf{u}$ represents latitudinal averages of $\bar{F}_{\text{MC},\theta}$ in the northern and southern hemispheres. For the vector \mathbf{b} , we have used the HK21 results, namely, $\mathbf{b} = (5 \times 10^{15}, -5 \times 10^{15})$

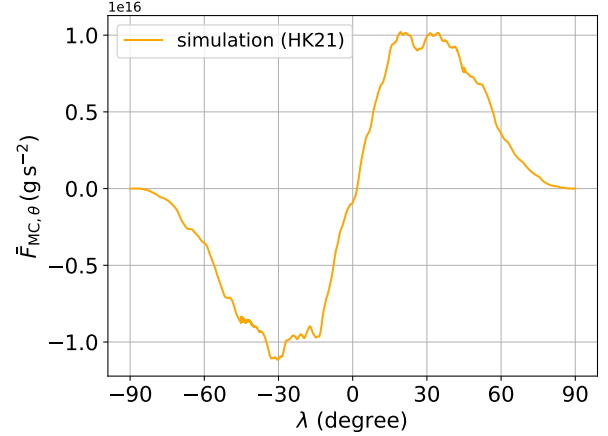


Figure 1. Latitudinal AM flux by MC that is radially averaged $\bar{F}_{\text{MC},\theta}(\theta)$ as a function of the latitude ($\lambda = \pi/2 - \theta$ where θ is the colatitude). The MC profile with the highest-resolution simulation in HK21 has been used to compute the AM flux (see Equation (C22)). Note that the positive $\bar{F}_{\text{MC},\theta}(\theta)$ indicates that the AM flows in the direction with the larger colatitude; that is, the AM is transported southward (northward) in the northern (southern) hemisphere if we take $\theta = 0$ as the northern pole.

in units of g s^{-2} . Note that we do not find any significant difference in the large-scale morphologies of inferred MC profiles even when we change the values of the elements in the vector \mathbf{b} by a few orders, as discussed in Section 5.1.

Second, to ensure the equatorward AM fluxes at almost all the latitudes, we further assume that $\bar{F}_{\text{MC},\theta}(\theta)$ is not rapidly varying in the latitudinal direction (see Figure 1). We thus consider a regularization term $D_{\text{HK2}} \mathbf{u}$ that represents the latitudinal derivative of $\bar{F}_{\text{MC},\theta}(\theta)$. The regularization matrix D_{HK2} is an $N_\theta \times 2N_j$ matrix where N_θ is the number of grid points in the latitudinal direction. We present how to compute the matrices D_{HK1} and D_{HK2} in Appendix C.

When considering the new constraints on AM transport by MC, the quantity to be minimized is:

$$X'_{\text{HK}} = |E^{-1/2}(\boldsymbol{\tau} - K\mathbf{u})|^2 + \alpha |D\mathbf{u}|^2 + \boldsymbol{\kappa} \cdot C\mathbf{u} + \boldsymbol{\mu} \cdot S\mathbf{u} + \beta |D_{\text{HK1}}\mathbf{u} - \mathbf{b}|^2 + \gamma |D_{\text{HK2}}\mathbf{u}|^2, \quad (14)$$

where new trade-off parameters β and γ have been introduced. Note that the new constraints are taken as regularization terms rather than strict constraints; hence, we must check whether a solution obtained with a certain set of trade-off parameters satisfies the constraints, as explained in Section 3.3. The solution for the minimization of X'_{HK} can be obtained by solving the following matrix equation (in almost the same way as that when

we have derived Equation (10)):

$$\begin{pmatrix} A' & C^T & S^T \\ C & O & O \\ S & O & O \end{pmatrix} \begin{pmatrix} \mathbf{u} \\ \boldsymbol{\kappa} \\ \boldsymbol{\mu} \end{pmatrix} = \begin{pmatrix} K^T E^{-1} \boldsymbol{\tau} + \beta D_{\text{HK1}}^T \mathbf{b} \\ \mathbf{0} \\ \mathbf{0} \end{pmatrix}, \quad (15)$$

where we have introduced a $2N_j \times 2N_j$ submatrix A' that is defined as:

$$A' = A + \beta D_{\text{HK1}}^T D_{\text{HK1}} + \gamma D_{\text{HK2}}^T D_{\text{HK2}} \quad (16)$$

(see Equation (11) for the definition of A). It should be noted that in addition to the $2N_j$ -dimensional data vector $K^T E^{-1} \boldsymbol{\tau}$, we have an extra $2N_j$ -dimensional vector $\beta D_{\text{HK}}^T \mathbf{b}$ on the right-hand side of Equation (15) that originates from the regularization term newly introduced. The solution thus obtained is shown later in Section 4.

3.3. How to determine values of the trade-off parameters and choose reasonable solutions

As described in Sections 3.1 and 3.2, once we determine values of the trade-off parameters, the RLS solution for Equation (3) with the HK21-type constraint can be obtained by solving the matrix equation (15). Here, we present how we determined the values of the trade-off parameters among numerous possible parameters. We will hereafter call the solutions thus obtained “reasonable solutions.”

First, we prepare a grid of the trade-off parameters. In the case of the HK21 regime, the decimal logarithms of α , β , and γ range from -3.5 to -2 , from -34 to -26 , and from -36 to -27 , respectively. Note the units of the trade-off parameters; that is, we express r , ρ , and \mathbf{U} in units of m, g m^{-3} , and m s^{-1} , respectively. The range of α is determined following the G20 results, and those of β and γ are chosen so that the inverse problem (3) is well-posed. For each set of the trade-off parameters in the prepared grid, we obtain the corresponding solution by solving Equation (15). We denote the solution thus obtained by $\hat{\mathbf{u}}_{\text{cand}}$.

Among the candidate solutions $\hat{\mathbf{u}}_{\text{cand}}$, we have chosen reasonable solutions based on the following two criteria. The first criterion is whether a candidate solution satisfies the constraint we have assigned in Section 3.2. We need this criterion because what we have imposed on the inverse problem (Equation (3)) is not a strict constraint but regularization (see Section 3.2). Specifically, when we consider the HK21-type constraint, we exclude candidate solutions that exhibit poleward $\bar{F}_{\text{MC},\theta}(\theta)$ in either hemisphere.

The second criterion is whether we can distinguish the large-scale morphology of an inferred MC profile,

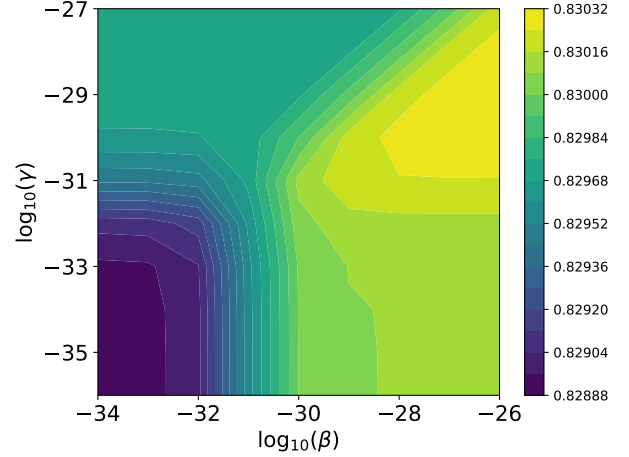


Figure 2. Trade-off plane obtained via MC inversion with the HK21-type constraint, which shows the residual term $|E^{-1/2}(\boldsymbol{\tau} - K\hat{\mathbf{u}}_{\text{cand}})|^2/N_d$ as a function of the decimal logarithms of the trade-off parameters β (horizontal axis) and γ (vertical axis) for $\alpha = 10^{-3}$. The brighter colors correspond to larger values of the residual term. See the main text for the meanings of the variables.

namely, a single- or multiple-cell structure, with 2σ significance. Estimated uncertainties are evaluated by introducing a $2N_j \times N_d$ matrix R_{cand} with which $\hat{\mathbf{u}}_{\text{cand}} = R_{\text{cand}} \boldsymbol{\tau}$. The uncertainty of the i -th component in $\hat{\mathbf{u}}_{\text{cand}}$ is then:

$$\delta(\hat{\mathbf{u}}_{\text{cand}})_i = \left(\sum_{j,k} (R_{\text{cand}})_{ij} E_{jk} (R_{\text{cand}})_{ik} \right)^{\frac{1}{2}}, \quad (17)$$

based on which estimated uncertainties for the meridional flow field (that is computed by using $\hat{\mathbf{u}}_{\text{cand}}$ as expansion coefficients, see Equation (2)) can be calculated.

In the next section, we show some of the reasonable solutions and the corresponding sets of trade-off parameters. It should be noted that we have not determined the most appropriate solution among the reasonable ones, which is in principle possible by, for example, selecting a solution that realizes a minimum residual term (see the first term of the right-hand side in, e.g., Equation (6)). The reason why we are satisfied with just the reasonable solutions is that the goal of this paper is to infer the large-scale morphology of the MC profile rather than to determine detailed structures of the meridional flow field. It is worth mentioning that the results show slight differences in the MC profiles of the reasonable solutions, highlighting little relevance of an attempt to find the “most appropriate” solution in this study.

4. RESULTS

With the data and method presented in Sections 2 and 3, we have carried out inversion to infer the solar MC

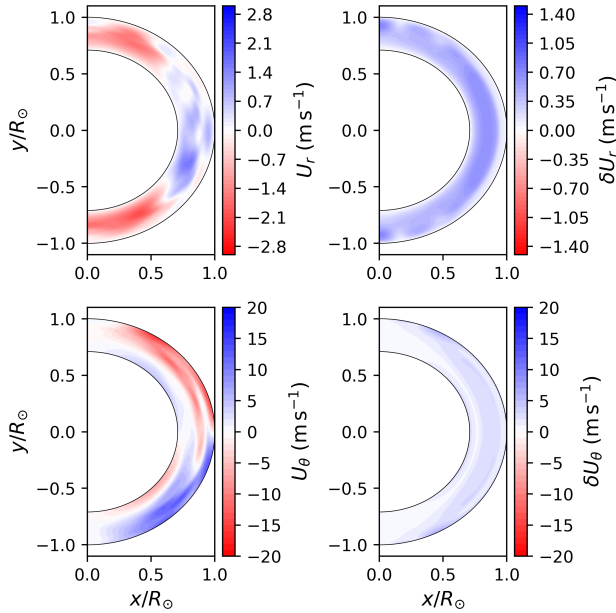


Figure 3. Meridional flow fields in units of m s^{-1} (left panels) and the estimated uncertainties that are determined by Equation (17) (right panels) in a meridional plane. The results are obtained via MC inversion without the HK21-type constraint, that corresponds to G20 results. The trade-off parameter $\alpha = 10^{-3}$, $\beta = 0$, and $\gamma = 0$ are used. The 2-dimensional Cartesian coordinate (x, y) is used to express the meridional plane where the convective boundaries are indicated by the black curves. The upper-left panel shows the radial component of the inferred meridional flow field U_r where red and blue indicate radially inward and outward motions, respectively. The lower-left panel shows the latitudinal component of the inferred meridional flow field U_θ in which red and blue indicate poleward and equatorward motions, respectively. A single-cell MC profile has been inferred, as has already been found by G20 (see, e.g., Figure 2a in G20). Note that we have adopted the assumption that MC is confined in the convective zone; thus, the velocity is zero elsewhere in the radiative zone below the convective zone ($r/R_\odot < 0.71$).

profile. In this section, we show inversion results thus obtained. We firstly show a trade-off relation to see an extent to which residuals vary with trade-off parameters (Section 4.1). Secondly, we present examples of reasonable solutions obtained with or without the HK21-type constraint (Section 4.2). We then compare the inferred MC profiles in Section 4.3. The inversion results are available at <https://doi.org/10.5281/zenodo.10893108> (Hatta et al. 2024).

4.1. Trade-off relation

A trade-off relation between the minimization of the residual term (i.e., the first term in the right-hand side of Equation (14)) and regularization (as represented by the second, fifth, and sixth terms in the right-hand side of

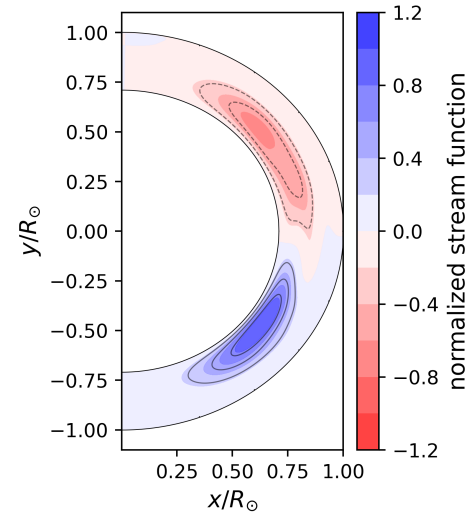


Figure 4. Normalized mass flux stream function (Equation A1) computed based on the single-cell MC profile that is inferred without the HK21-type constraint. A red (blue) region with dashed (solid) contours indicates counterclockwise (clockwise) motion. Both hemispheres possess a single cell structure in the radial direction.

Equation (14)) is useful for checking behaviors of candidate solutions $\hat{\mathbf{u}}_{\text{cand}}$ obtained for the prepared grid of the trade-off parameters (see Section 3.3). Figure 2 shows the contour map of the residual term divided by the number of the data ($|E^{-1/2}(\boldsymbol{\tau} - K\hat{\mathbf{u}}_{\text{cand}})|^2/N_d$) as a function of the trade-off parameters β and γ for $\alpha = 10^{-3}$. Basically, the residual term increases as β or γ increases. This results from the fact that as we increase the trade-off parameters, minimizing the corresponding regularization terms is more prioritized over minimizing the residual term, as we mentioned in Section 3.1 (see also Equation (14)). We find the same (β, γ) dependence of the residual term in the case of other values of α , in which the absolute value of the residual becomes smaller (larger) when α becomes smaller (larger).

Another feature found in the trade-off planes is a non-monotonous behavior of the residual with respect to γ for fixed α and β . In particular, the residual is not monotonic in terms of γ when $\beta > 10^{-30}$, for which we give some explanation. We first focus on the dependence of the residual on β for a fixed γ . It is readily noticed that the residual is monotonically increasing in terms of β . As shown later in this section, the increasing residual is accompanied by a transition in the averaged AM flux by MC from the poleward one to equatorward one; roughly speaking, $D_{\text{HK1}}\hat{\mathbf{u}}_{\text{cand}} \parallel -\mathbf{b}$ for $\beta < 10^{-30}$ and $D_{\text{HK1}}\hat{\mathbf{u}}_{\text{cand}} \sim \mathbf{b}$ for $\beta > 10^{-30}$ (see Section 3.2 for the definitions of D_{HK1} and \mathbf{b}). This trend can be in-

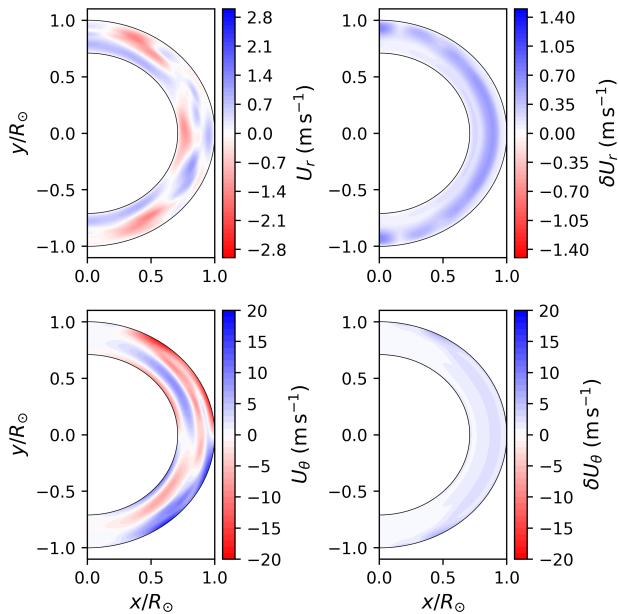


Figure 5. Same as Figure 3 except that the inversion results were obtained with the constraint on AM transport by MC, namely, $\alpha = 10^{-3}$, $\beta = 10^{-30}$, and $\gamma = 10^{-31}$, are shown.

terpreted as evidence that an estimated MC profile with stronger equatorward AM transport is related to a larger residual. Keeping that in mind, let us then focus on the dependence of the residual on γ (see, e.g., $\beta = 10^{-28}$ in Figure 2). When γ is small ($\gamma < 10^{-31}$), β is a dominant trade-off parameter; thus, the residual increases with the increasing γ (which is a typical trend as discussed in the previous paragraph) while achieving the equatorward AM transport by MC ($D_{\text{HK1}} \hat{\mathbf{u}}_{\text{cand}} \sim \mathbf{b}$). However, γ becomes dominant when $\gamma > 10^{-30}$, prioritizing minimization of the latitudinal derivative of $\bar{F}_{\text{MC},\theta}(\theta)$, eventually leading to a flat solution with $\bar{F}_{\text{MC},\theta}(\theta) \sim 0$ in the limit $\gamma \rightarrow \infty$ where $D_{\text{HK1}} \hat{\mathbf{u}}_{\text{cand}} \sim \mathbf{0}$. The results show that for $\gamma > 10^{-30}$, the averaged AM flux by MC transitions from equatorward to 0 as γ becomes larger, corresponding to smaller residuals as we discussed the β dependence of the residual for a fixed γ .

4.2. Examples of inferred MC profiles

We move on to the reasonable solutions for MC inversion chosen based on the procedure described in Section 3.3. We first show an example of the results of MC inversion without any constraints on AM transport by MC, namely, $\beta = \gamma = 0$ (the other trade-off parameter α is set to be 10^{-3}). That corresponds to MC inversion carried out by G20. We thus expect the G20 result, and indeed, we have confirmed it; that is, there is an equatorward flow at the base of the convective zone, and the

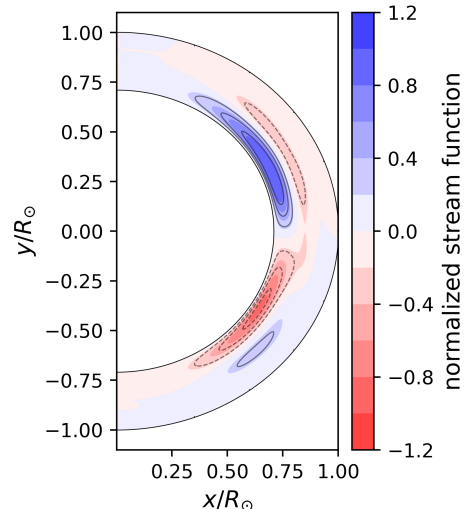


Figure 6. Same as Figure 4, but in the case of the MC profile inferred with the constraint on AM transport by MC. Each hemisphere has two cells.

sign of the radial component of the meridional flow field (U_r) is unchanged at most of the latitudes (Figure 3); thus, the single-cell MC profile has been inferred (Figure 4).

Then, we present inversion results obtained with the HK21-type constraint. Figure 5 shows an example of the inferred MC profiles for which the trade-off parameters $\alpha = 10^{-3}$, $\beta = 10^{-30}$, and $\gamma = 10^{-31}$ are used. The prominent features are that there is a poleward flow at the base of the convective zone and that the radial component of the meridional flow changes the sign in the radial direction for all the latitudes, indicating a double-cell MC profile. The double-cell structure can be confirmed as well by taking a look at the stream function (Figure 6) that shows each hemisphere has two cells in the radial direction, although there is a contrast between the deeper and shallower cells. We would like to emphasize that all the reasonable solutions have exhibited the double-cell structure. As a whole, MC inversion with the HK21-type constraint results in a double-cell MC profile, which is different from the G20 result.

4.3. Comparison of the inferred MC profiles

To see the difference between the inferred single- and double-cell MC profiles more quantitatively, we present slices of the latitudinal component of the inferred meridional flow field (U_θ) at certain radii ($r = r_{\text{czb}}$ or R_\odot) and latitudes ($|\lambda| = 30$ or 45 degrees) (Figure 7). It is seen that, in both MC profiles, the inferred surface MC velocity (~ 10 – 20 m s^{-1}) is compatible with the results of surface observations (e.g. Hathaway 1996). However, we

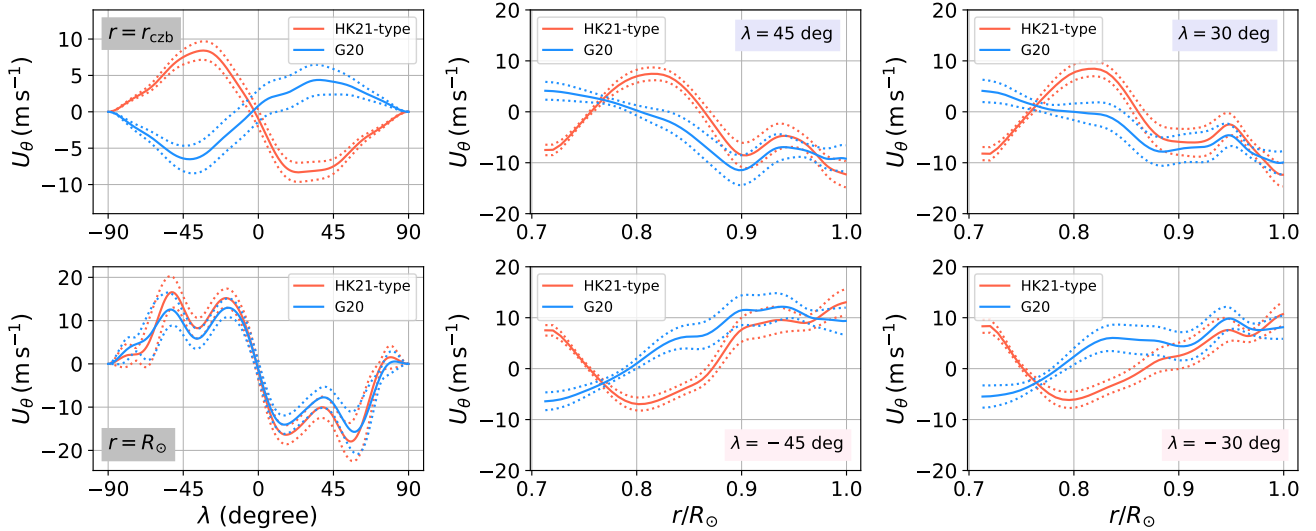


Figure 7. Slices of the latitudinal component of the meridional flow field U_θ inferred with and without the HK21-type constraint (red and blue, respectively). The upper-left and lower-left panels show the slices at the bottom of the convective zone ($r = r_{\text{czb}}$) and the surface $r = R_\odot$, respectively. The middle and right panels show the slices at certain latitudes, namely, $\lambda = 45$ degrees (upper-middle), $\lambda = -45$ degrees (lower-middle), $\lambda = 30$ degrees (upper-right), and $\lambda = -30$ degrees (lower-right), respectively. Dashed curves indicate 1σ uncertainties that are evaluated with Equation (17).

notice a clear difference in the flow profiles in a deeper region, especially around the base of the convective zone. The inferred single-cell MC profile there is characterized by an equatorward flow whose velocity amplitude is relatively small ($< 5 \text{ m s}^{-1}$; see the upper-left panel in Figure 7). In contrast, in the case of the double-cell MC profile, we find a fairly fast poleward flow ($\sim 8\text{--}9 \text{ m s}^{-1}$) whose velocity is even comparable to the surface one at some latitudes.

Another obvious difference between the single- and double-cell MC profiles is the thickness of the subsurface poleward flow (see, e.g., the upper-middle panel in Figure 7). The single-cell MC profile exhibits the subsurface poleward flow that reaches around $r/R_\odot \sim 0.8$, whereas that of the double-cell profile is thinner and reaches a shallower depth ($r/R_\odot > 0.85$).

The differences between the inferred flow profiles are closely related to differences in (the latitudinal component of) the mass/AM flux by MC (Figure 8). We first consider the mass flux (ρU_θ). The net mass flux is zero at an arbitrary colatitude since we assume the mass conservation in this study. Therefore, in the case of the single-cell MC profile, the equatorward mass flux around the base of the convective zone is balanced with the poleward mass flux in the outer envelope (see the upper-right panel in Figure 8). This is opposite to the case of the double-cell MC profile in which the poleward mass flux in the deep convective zone is nearly balanced with the equatorward mass flux in the middle of the con-

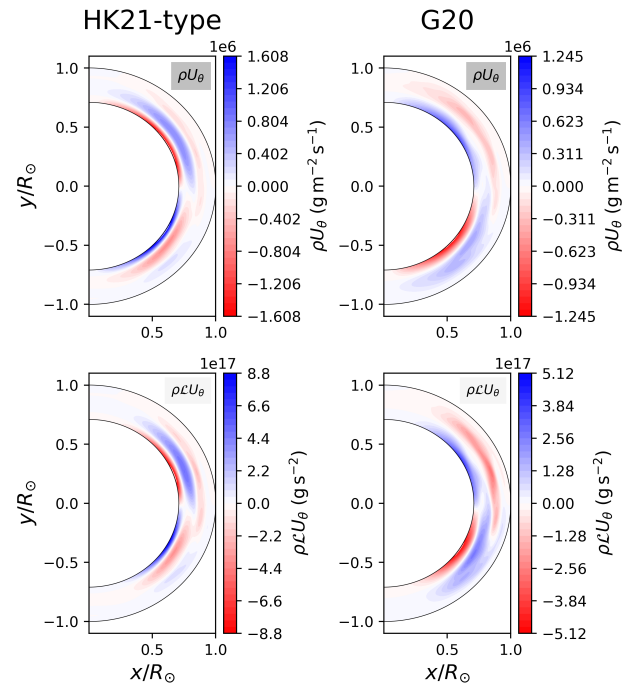


Figure 8. Mass flux ρU_θ (upper panels) and AM flux $\rho \mathcal{L} U_\theta$ (lower panels) calculated with the latitudinal component of the inferred meridional flow fields U_θ (lower-left panels in Figures 3 and 5). Red (blue) indicates the northward (southward) flux. See Appendix C for how ρ and \mathcal{L} were computed.

vective zone; it should be noted that another poleward

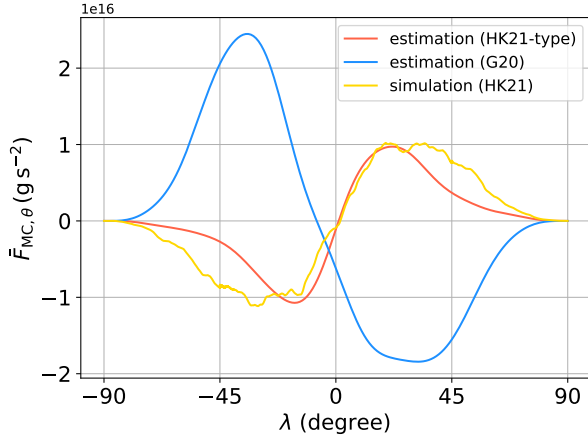


Figure 9. Same as Figure 1 except that the averaged AM fluxes computed based on the inferred single- and double-cell MC profiles (Figures 3 and 5) have been included (blue and red, respectively). For the HK21-type constraint, $\mathbf{b} = (5 \times 10^{15}, -5 \times 10^{15})$ in units of g s^{-2} has been adopted (see Equation 13) based on the numerical results of HK21.

mass flux in the outermost zone is negligible due to the density stratification inside the Sun (see the upper-left panel in Figure 8).

As for the AM flux ($\rho \mathcal{L} U_\theta$), it is apparent that the AM flux profile is similar to that of the mass flux (ρU_θ) (compare the lower and upper panels in Figure 8). However, the net AM flux is not zero due to the proportionality $\mathcal{L} \propto r^2$. More specifically, in the case of the single-cell (double-cell) MC profile, the outer poleward (equatorward) AM flux is dominant over the inner equatorward (poleward) AM flux and the net AM flux by MC is poleward (equatorward) (Figure 9). In fact, it can be shown that the net AM flux by MC is always poleward when the MC profile is single-cell, which is detailed later in Section 5.1.

Finally, we briefly remark on the values of the residual terms $|E^{-1/2}(\boldsymbol{\tau} - K\hat{\mathbf{u}})|^2/N_d$ in the cases of the single- and double-cell MC profiles. As seen in the trade-off plane for $\alpha = 10^{-3}$ (Figure 2), the single-cell profile, which corresponds to the set of the trade-off parameters $(\beta, \gamma) \rightarrow (0, 0)$, exhibits a smaller residual (~ 0.8288) than the double-cell profile, which corresponds to the set of the trade-off parameters $(\beta, \gamma) = (10^{-30}, 10^{-31})$, (~ 0.8300). There is nevertheless just a 0.1% difference between the residuals; thus, both profiles explain the data more or less at the same level. It should also be instructive to mention that the residual is dependent on α as well, and we have found a number of α as reasonable values for the trade-off parameter with which the residual could vary more than the $\sim 0.1\%$ difference mentioned. Therefore, based on the size of the residuals

alone, it is difficult to favor or disfavor either of the MC profiles at the moment. We discuss details on inversion results from a different perspective later in Section 5.4.

5. DISCUSSION

In this section, we discuss the inversion results obtained in Section 4. We firstly assess, from theoretical perspectives, the result of the double-cell MC profile inferred with the HK21-type constraint focusing on AM and magnetic field transport by MC (Sections 5.1 and 5.2, respectively). We then look for possible MC profiles based on an assumption that the Reynolds stress is a dominant source for the latitudinal AM transport (RS regime), though it is in a rather crude manner (Section 5.3). Finally, all of the MC profiles inferred in this study are compared (Section 5.4).

5.1. Latitudinal AM transport by single-cell MC is always poleward

In Section 4, the double-cell MC profile has been inferred based on inversion with a constraint that the latitudinal AM transport by MC should be equatorward. Actually, this is expected. An important point is that when we assume mass conservation and $U_\theta = 0$ at the poles, which are adopted as the strict constraints in this study (see Section 3.1), AM transport by single-cell MC is always poleward. The reason is explained in the following paragraphs.

We here consider a single-cell MC in the northern hemisphere where the meridional flow is poleward (equatorward) in the outer (inner) convective zone. Let us then start with the surface integral of the mass flux at an arbitrary colatitude θ that is defined as

$$M_{\text{net}} = \int_{r_{\text{czb}}}^{R_\odot} \int_0^{2\pi} \rho U_\theta r \sin \theta \, d\phi \, dr,$$

where ϕ is the azimuthal angle in the spherical coordinate. The surface integral M_{net} is zero because of the assumptions of the mass conservation and $U_\theta = 0$ at the poles. If we take a point inside the convective zone at which U_θ changes the sign ($r = r_0$), the previous argument can be expressed as $M_{\text{net}} = M_{\text{in}} + M_{\text{out}} = 0$, where

$$M_{\text{in}} = (2\pi \sin \theta) \int_{r_{\text{czb}}}^{r_0} \rho U_\theta r \, dr,$$

and

$$M_{\text{out}} = (2\pi \sin \theta) \int_{r_0}^{R_\odot} \rho U_\theta r \, dr.$$

Then, we focus on the surface integral of the AM flux at the same colatitude that can be expressed as $L_{\text{net}} = L_{\text{in}} + L_{\text{out}}$, where

$$L_{\text{in}} = (2\pi \sin \theta) \int_{r_{\text{czb}}}^{r_0} \rho \mathcal{L} U_\theta r \, dr,$$

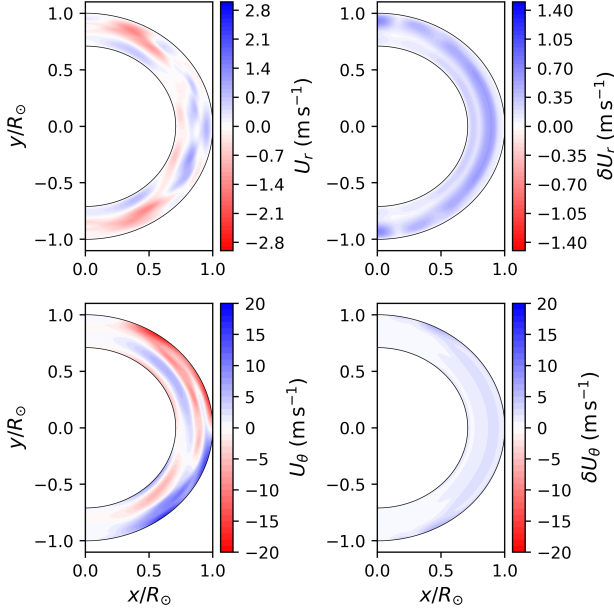


Figure 10. Same as Figure 5 except that we have weakened the constraint on AM transport by MC by requiring a small amount of the equatorward AM transport (\sim a hundredth of that found in HK21). The trade-off parameters $\alpha = 10^{-3}$, $\beta = 10^{-28}$, and $\gamma = 10^{-29}$ are used. A double-cell MC profile has been inferred even with the constraint that there is just tiny equatorward AM transport by MC.

and

$$L_{\text{out}} = (2\pi \sin \theta) \int_{r_0}^{R_{\odot}} \rho \mathcal{L} U_{\theta} r dr.$$

When we denote the specific AM at $r = r_0$ by \mathcal{L}_0 , we have

$$0 < L_{\text{in}} < \mathcal{L}_0 \times M_{\text{in}},$$

and

$$L_{\text{out}} < \mathcal{L}_0 \times M_{\text{out}} < 0.$$

This is because \mathcal{L} is monotonically increasing in the radial direction (Miesch & Hindman 2011), and $\mathcal{L} < \mathcal{L}_0$ ($\mathcal{L} > \mathcal{L}_0$) in the inner (outer) convective zone by definition of \mathcal{L}_0 . Note also that M_{in} (M_{out}) is positive (negative) in the northern hemisphere. Remembering the definition of L_{net} , we have the following relation:

$$L_{\text{net}} = L_{\text{in}} + L_{\text{out}} < \mathcal{L}_0(M_{\text{in}} + M_{\text{out}}) = 0,$$

showing that the net latitudinal AM transport by MC is negative in the northern hemisphere. Likewise, L_{net} is positive in the southern hemisphere; that is, AM transport by MC is always poleward in the case of the single-cell MC profile.

Overall, the poleward AM transport by MC, which is inevitable when the MC profile is a single-cell structure,

is incompatible with the HK21-type constraint that AM transport by MC should be equatorward. This is the reason why we have not obtained a single-cell MC profile via inversion with the HK21-type constraint despite the fact that we have used the same dataset as that used in G20 who have obtained a single-cell MC profile. We have confirmed that the double-cell MC profile has been inferred even when we require a small amount of AM transport by MC (\sim a hundredth of that found in HK21) (Figure 10). Therefore, if the physics in the HK21 regime correctly describes the cause of the solar equator-fast rotation, it is plausible that the MC profile is a double-cell structure (or it might be multiple-cell that cannot be ruled out because of the low resolution of MC inversion currently available; see also discussions in Fuentes et al. 2024).

5.2. How about magnetic field transport by MC?

We may discuss not only AM transport but also magnetic field transport inside the convective zone based on the inferred MC profiles. For example, G20 have found that the single-cell MC can reproduce the 11-year periodic sunspot migration by considering the flux transport dynamo and assuming that magnetic fields are generated at the base of the convective zone. In their framework, the double-cell MC profile cannot explain the equatorward sunspot migration since the magnetic fields generated at the base of the convective zone are transported toward the poles by the poleward meridional flow there.

Is the single-cell MC profile preferable to the double-cell profile in terms of the magnetic field transport by MC? This is not necessarily the case. One possible scenario for the equatorward sunspot migration by the double-cell MC is that magnetic fields are generated in the middle of the convective zone where they are transported by the equatorward meridional flow (e.g. Nelson et al. 2013). Alternatively, instead of the flux transport dynamo, we can reproduce the equatorward sunspot migration by considering the turbulent α effect if the sign of α is negative around the tachocline (Parker 1955; Yoshimura 1975). It is thus not straightforward to draw some conclusions on the morphology of the MC profile solely based on magnetic field transport by MC.

5.3. What if AM transport by Reynolds stress dominates over AM transport by MC?

As described in Section 1, not only the HK21 regime but also the RS regime allows us to reproduce the solar equator-fast rotation (e.g. Featherstone & Miesch 2015, hereafter FM15). In this section, in order to discuss MC profiles possible in the RS regime, we attempt to carry out MC inversion with the RS-type constraint.

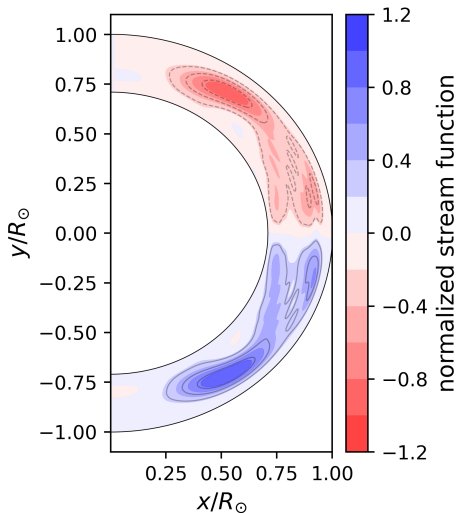


Figure 11. Same as Figure 4, but in the case of the MC profile inferred via MC inversion with the RS-type constraint (see the main text, Appendix A, and Appendix B for more details). The mass flux stream function is characterized by the cylindrical (single-cell) profile in the low-(high-)latitude region, which is similar to that found in the numerical simulations in the RS regime (see, e.g., Figure 6c in FM15).

In the RS regime, the magnetic field is not dominant in AM redistribution and the equator-fast rotation is achieved by the turbulent AM transport (e.g., FM15). It is not straightforward to devise constraints on the MC profile because there is no linear relation between the meridional flow and Reynolds stress profile. Therefore, instead of physics constraints devised based on the numerical results found in the RS regime, we consider qualitative and topological constraints that are appropriate for this regime. We especially focus on a result that the stream function of the mass flux behaves differently in the low-latitude region and high-latitude region; it is cylindrical for $|\lambda| < 40$ degrees and single-cell for $|\lambda| > 40$ degrees, where λ is the latitude (see, e.g., Figures 4 and 6 in FM15). We can then separately devise constraints for the low- and high-latitude regions (more details can be found in Appendix A). Reasonable solutions have been chosen based on the same criteria as described in Section 3.3.

Figure 11 shows the mass flux stream function of the MC profile thus inferred. The stream function is a single-cell structure in the high-latitude region and cylindrical in the low-latitude region, resembling the result of numerical simulations in the RS regime (see, e.g., Figure 6c in FM15). More details on the inversion results obtained with the qualitative constraint can be found in Appendix B.

A typical value of the residual terms computed with the reasonable solutions found for the RS regime is larger than those we have found in Section 4 by $\sim 0.5\%$. This probably reflects the fact that it is more difficult for us to explain the data based on an assumption that MC profiles should be similar to those found in FM15 compared with the assumptions of the single- or double-cell MC profiles.

5.4. Comparison of the inversion results based on averaging kernels

In order to compare the inversion results obtained in this study more carefully, we introduce the averaging kernel. In the RLS method, estimates can be expressed as linear combinations of data. For instance, an estimate of the latitudinal component of the meridional flow field at a certain target point $(r, \theta) = (r_t, \theta_t)$ is given as:

$$\hat{U}_\theta(r_t, \theta_t) = \sum_{i=1}^{N_d} c_i(r_t, \theta_t) \tau_i, \quad (18)$$

where c_i is the inversion coefficient for the target point that is determined by inverting the matrix equation such as Equation (10). Substituting Equation (1) for Equation (18) leads to the following expression:

$$\begin{aligned} \hat{U}_\theta(r_t, \theta_t) = & \\ & \iint (D_r(r, \theta; r_t, \theta_t) U_r(r, \theta) + D_\theta(r, \theta; r_t, \theta_t) U_\theta(r, \theta)) dr d\theta \\ & + \sum_{i=1}^{N_d} c_i(r_t, \theta_t) e_i, \end{aligned} \quad (19)$$

where we have the averaging kernel,

$$D_\theta(r, \theta; r_t, \theta_t) = \sum_{i=1}^{N_d} c_i(r_t, \theta_t) \mathcal{K}_i^\theta(r, \theta), \quad (20)$$

and the cross-talk kernel,

$$D_r(r, \theta; r_t, \theta_t) = \sum_{i=1}^{N_d} c_i(r_t, \theta_t) \mathcal{K}_i^r(r, \theta). \quad (21)$$

The estimate \hat{U}_θ is thus considered as the sum of the mean U_r averaged by the cross-talk kernel and the mean U_θ averaged by the averaging kernel. We can evaluate the resolution of inversion and contamination in the estimate based on the averaging kernel and the cross-talk kernel, respectively.

We show the averaging kernels computed for the three different inversion results that correspond to the cylindrical, double-cell, and single-cell MC profiles (from top to bottom in Figure 12). Four depths ($r/R_\odot =$

0.72, 0.82, 0.93, and 0.98) at a latitude ($\lambda = 30$ degrees) are selected as target points. Because we have confirmed that the cross-talk term (see the first term in Equation (19)) contributes little to the estimate in each case, only the averaging kernels are shown in the figure.

It is evident that, in the case that we have obtained the cylindrical MC profile (see the top row in Figure 12), the averaging kernels are well localized only in the shallow region ($r/R_\odot \sim 0.98$), and they have exhibited some oscillatory patterns elongated in the z -direction that may be caused by the constraint that the stream function should be cylindrical. We may find averaging kernels with better resolution as we weaken the RS-type constraint by reducing the value of the trade-off parameter, though in those cases we cannot reproduce the cylindrical MC profile. These properties indicate that MC inversion with the RS-type constraint is not working well compared with the other two cases (the middle and bottom rows in Figure 12).

Importantly, when we compare the averaging kernels computed for the other two inversion results (i.e., the middle and bottom rows in Figure 12), we notice that inversion with the single-cell solution performs better than that with the double-cell solution. For example, the resolved estimate can be obtained even around the middle of the convective zone ($r/R_\odot \sim 0.82$) in the case of inferring the single-cell MC profile (see the second left panel in the bottom row in Figure 12). The better performance in inversion with the single-cell solution is expected because the solution has been obtained with the smallest number of the constraints. In contrast, in the case with the HK21-type constraint, there is a contribution of the extra term $\beta D_{\text{HK1}}^T \mathbf{b}$ (see the right-hand side of Equation (15)) to the estimate that becomes comparable to half the estimate around the base of the convective zone. The resolution of averaging kernels targeting around $r/R_\odot \sim 0.82$ can be improved by reducing the value of the trade-off parameter β , although equatorward AM transport by MC cannot be established in such cases, as we discussed the resolution of the averaging kernels computed for the cylindrical MC profile. Thus, the estimates in the deeper region are significantly affected by the extra term.

Then, in terms of how well the localization is done, the solution with the single-cell MC profile seems to be the most appropriate among the inversion results obtained in this study. Please note, however, that the main purpose of this study is to evaluate how MC inversion is affected when we adopt the assumption that the HK21 regime correctly describes physics in the solar convective zone. We thus cannot conclude that the MC profile

is single-cell, based on the resolution of the averaging kernels alone.

Although we have seen in Section 5.1 that the single-cell MC profile cannot be inferred via inversion with the HK21-type constraint, there is no such restriction in the RS regime. FM15 discuss the possibility that the single-cell MC profile could be realized if the Reynolds stress is strong enough to overcome the poleward transport AM by MC (see Figure 13 in FM15). Thus, as a summary of the inversion results obtained in this study, we would like to suggest two possibilities: the HK21 regime is correct, and the double-cell MC profile sustains the equator-fast rotation; or the RS regime is correct, and the poleward AM transport by the single-cell MC is overwhelmed by that of the Reynolds stress. One of the keys to narrowing down the possibilities is the understanding of the relation between the meridional flow field and the Reynolds stress profile that would provide us with a new physics constraint on MC inversion rather than the crude constraint we attempted in this section. We will investigate that point in the forthcoming paper.

We close this section with a brief comment on the results of MC inversion recently carried out by [Herczeg & Jackiewicz \(2023\)](#) (hereafter HJ23) based on Bayesian statistics. With G20's datasets, HJ23 have concluded that the MC profile is a single-cell structure in both the cycles 23 and 24 (see also Figure 5 in HJ23), which is different from our results. This may be because how we parameterize the MC profile is different from that in HJ23 (see Table 1 in HJ23). We also have a difference in the sensitivity kernels; that is, we have used the kernels computed based on Born approximation while HJ23 have used ones computed based on ray approximation. Some considerations would therefore be required to directly compare the results in this study with those in HJ23. A comprehensive comparison of possible parameterizations of the MC profile would be helpful for selecting the most probable MC profiles, which can be conducted via, for example, a Bayesian model comparison ([Gregory 2005](#)). That is another topic we will work on in the near future.

6. CONCLUSION

By carrying out inversion of the travel times measured by G20 with the constraint that AM transport by MC should be equatorward (the HK21-type constraint), we have inferred a double-cell MC profile. As the assumptions of the mass conservation and $U_\theta = 0$ at the poles require that the single-cell MC always transports the AM toward the poles, it is plausible that the MC profile is a double-cell structure *if AM transport by MC is equa-*

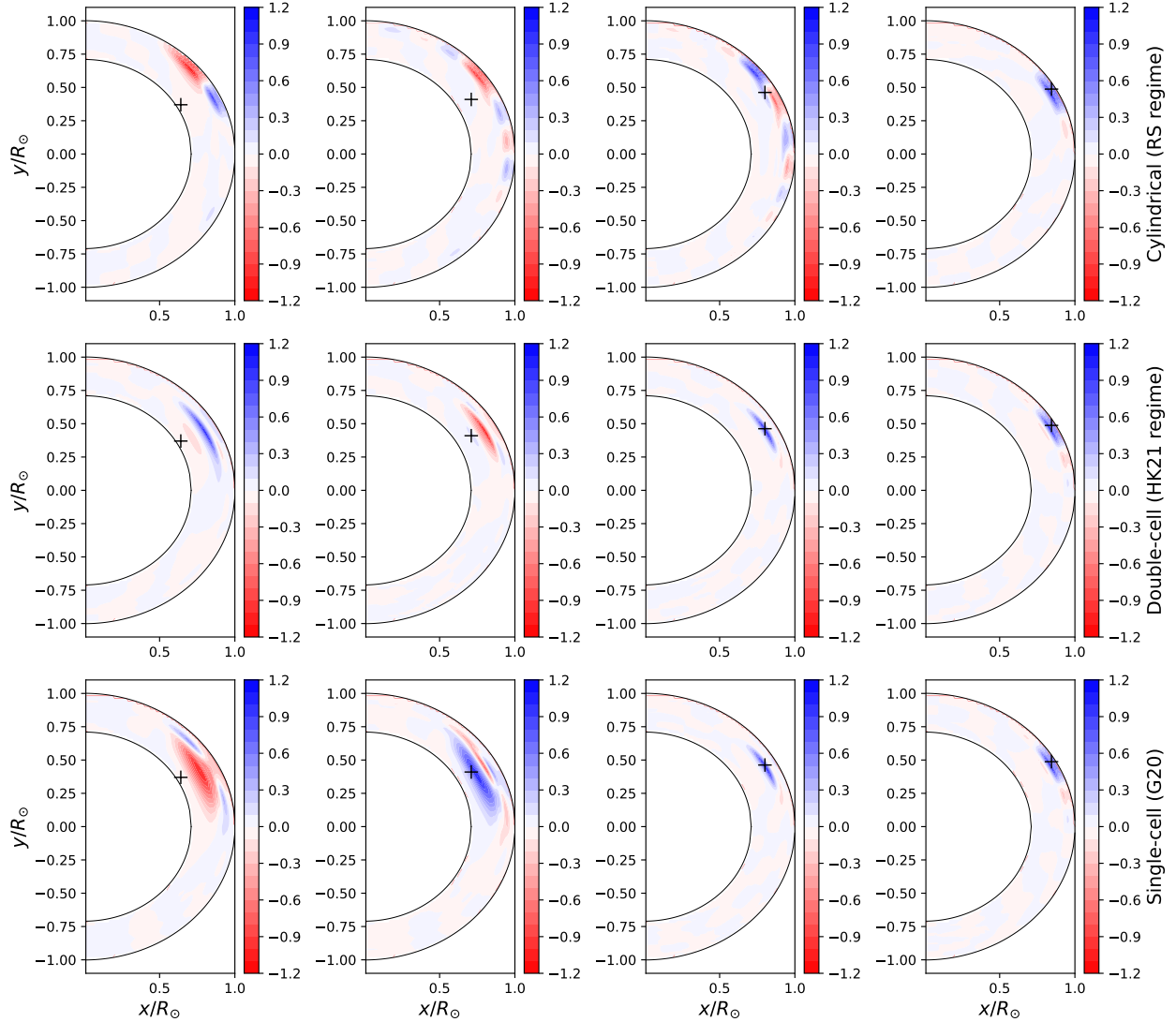


Figure 12. Averaging kernels for the inversion results obtained in this study. The top, middle, and bottom rows correspond to the RS-type constraint, HK21-type constraint, and the conventional constraints (Equations 7 and 8), respectively. Four depths ($r/R_{\odot} = 0.72, 0.82, 0.93,$ and 0.98) with a latitude ($\lambda = 30$ degrees) have been chosen as the target points that are indicated by black crosses. The target depth becomes deeper from right to left. Red and blue represent negative and positive values, respectively. Well-localized averaging kernels exhibit unimodal shapes with positive peaks (see, e.g., the second right panels in the middle and bottom rows) whereas those with poor resolution exhibit negative values and/or oscillatory patterns (see, e.g., the second left panel in the top row). It should also be noted that we sometimes see well-localized averaging kernels but the peak is far from the target point (see, e.g., the leftmost panel in the middle row); hence, the corresponding estimate is thus not considered as an appropriate spatial average around the target point. Note that the averaging kernels have been normalized for visual aid.

forward inside the Sun, as has been found in the HK21 regime.

In a rather crude manner, MC inversion with the RS-type constraint has been carried out, revealing the difficulty in explaining the G20 data based on the assumption of a cylindrical mass flux stream function that is found in numerical simulations in the RS regime. However, a comparison of the averaging kernels calculated for the inversion results obtained in this study indicates

that the best localization is achieved for the single-cell MC profile. There is thus a dilemma in our inversion, that is, putting more priority on the prior information (represented by the HK21-type constraint) leads us to a double-cell MC profile, whereas putting more priority on the resolution of the averaging kernels leads us to a single-cell MC profile. Overall, we have chosen to be conservative and not to conclude in this study that the MC profile is a double-cell structure.

It is theoretically considered that the single-cell MC profile could be established if AM transport by the Reynolds stress is fairly strong (RS regime). Because the HK21 and RS regimes are currently the only regimes in which the solar equator-fast rotation has been reproduced successfully (and MC inversion with the HK21-type constraint has been done in this paper), MC inversion with a genuine constraint on the Reynolds stress would be desirable for further investigating possible MC profiles in the solar convective zone.

ACKNOWLEDGEMENTS

We would like to express our gratitude to the authors of Gizon et al. (2020) who have made the datasets (Open Research Data Repository of the Max Planck Society) publicly available, enabling us to initiate this study. This work was supported by MEXT as “Program for Promoting Researches on the Supercomputer Fugaku” (grant numbers: J20HJ00016, JPMXP1020200109, JPMXP1020230406, and JPMXP1020230504), JSPS Grant-in-Aid for JSPS Research Fellow Grant Number JP23KJ0300, and JSPS KAKENHI grant numbers JP21H04497, JP21H01124, JP21H04492, and JP23H01210.

REFERENCES

- Bekki, Y., Cameron, R. H., & Gizon, L. 2024, *Science Advances*, 10, eadk5643, doi: [10.1126/sciadv.adk5643](https://doi.org/10.1126/sciadv.adk5643)
- Braun, D. C., & Birch, A. C. 2008, *ApJL*, 689, L161, doi: [10.1086/595884](https://doi.org/10.1086/595884)
- Charbonneau, P. 2020, *Living Reviews in Solar Physics*, 17, 4, doi: [10.1007/s41116-020-00025-6](https://doi.org/10.1007/s41116-020-00025-6)
- Chen, R., & Zhao, J. 2017, *ApJ*, 849, 144, doi: [10.3847/1538-4357/aa8eec](https://doi.org/10.3847/1538-4357/aa8eec)
- Chou, D.-Y., & Ladenkov, O. 2005, *ApJ*, 630, 1206, doi: [10.1086/432372](https://doi.org/10.1086/432372)
- Choudhuri, A. R., Schussler, M., & Dikpati, M. 1995, *A&A*, 303, L29
- Christensen-Dalsgaard, J., Dappen, W., Ajukov, S. V., et al. 1996, *Science*, 272, 1286, doi: [10.1126/science.272.5266.1286](https://doi.org/10.1126/science.272.5266.1286)
- Dikpati, M., & Charbonneau, P. 1999, *ApJ*, 518, 508, doi: [10.1086/307269](https://doi.org/10.1086/307269)
- Duvall, T. L., Jr., Jefferies, S. M., Harvey, J. W., & Pomerantz, M. A. 1993, *Nature*, 362, 430, doi: [10.1038/362430a0](https://doi.org/10.1038/362430a0)
- Featherstone, N., Anders, E. H., Augustson, K. C., et al. 2023, in *Bulletin of the American Astronomical Society*, Vol. 55, 105, doi: [10.3847/25c2feb.240cbaca](https://doi.org/10.3847/25c2feb.240cbaca)
- Featherstone, N. A., & Miesch, M. S. 2015, *ApJ*, 804, 67, doi: [10.1088/0004-637X/804/1/67](https://doi.org/10.1088/0004-637X/804/1/67)
- Fournier, D., Gizon, L., Hohage, T., & Birch, A. C. 2014, *A&A*, 567, A137, doi: [10.1051/0004-6361/201423580](https://doi.org/10.1051/0004-6361/201423580)
- Fournier, D., Hanson, C. S., Gizon, L., & Barucq, H. 2018, *A&A*, 616, A156, doi: [10.1051/0004-6361/201833206](https://doi.org/10.1051/0004-6361/201833206)
- Fuentes, J. R., Hindman, B. W., Zhao, J., et al. 2024, *ApJ*, 961, 78, doi: [10.3847/1538-4357/ad13f3](https://doi.org/10.3847/1538-4357/ad13f3)
- Gastine, T., Yadav, R. K., Morin, J., Reiners, A., & Wicht, J. 2014, *MNRAS*, 438, L76, doi: [10.1093/mnras/slt162](https://doi.org/10.1093/mnras/slt162)
- Giles, P. M. 2000, PhD thesis, Stanford University, California
- Giles, P. M., Duvall, T. L., Scherrer, P. H., & Bogart, R. S. 1997, *Nature*, 390, 52, doi: [10.1038/36294](https://doi.org/10.1038/36294)
- Gizon, L., & Birch, A. C. 2002, *ApJ*, 571, 966, doi: [10.1086/340015](https://doi.org/10.1086/340015)
- . 2004, *ApJ*, 614, 472, doi: [10.1086/423367](https://doi.org/10.1086/423367)
- Gizon, L., Birch, A. C., & Spruit, H. C. 2010, *ARA&A*, 48, 289, doi: [10.1146/annurev-astro-082708-101722](https://doi.org/10.1146/annurev-astro-082708-101722)
- Gizon, L., Cameron, R., Pourabdian, M., et al. 2020, Meridional flow in the Sun’s convection zone is a single cell in each hemisphere, V1, Edmond, doi: [10.17617/3.NAPBUA](https://doi.org/10.17617/3.NAPBUA)
- Gizon, L., Cameron, R. H., Pourabdian, M., et al. 2020, *Science*, 368, 1469, doi: [10.1126/science.aaz7119](https://doi.org/10.1126/science.aaz7119)
- Gizon, L., Barucq, H., Duruflé, M., et al. 2017, *A&A*, 600, A35, doi: [10.1051/0004-6361/201629470](https://doi.org/10.1051/0004-6361/201629470)
- Gizon, L., Cameron, R. H., Bekki, Y., et al. 2021, *A&A*, 652, L6, doi: [10.1051/0004-6361/202141462](https://doi.org/10.1051/0004-6361/202141462)
- Gregory, P. C. 2005, *Bayesian Logical Data Analysis for the Physical Sciences: A Comparative Approach with ‘Mathematica’ Support*
- Hanasoge, S. M. 2022, *Living Reviews in Solar Physics*, 19, 3, doi: [10.1007/s41116-022-00034-7](https://doi.org/10.1007/s41116-022-00034-7)
- Hathaway, D. H. 1996, *ApJ*, 460, 1027, doi: [10.1086/177029](https://doi.org/10.1086/177029)
- Hatta, Y., Hotta, H., & Sekii, T. 2024, Inversion for Inferring Solar Meridional Circulation: The Case with Constraints on Angular Momentum Transport inside the Sun, Zenodo, doi: [10.5281/zenodo.10893108](https://doi.org/10.5281/zenodo.10893108)
- Hecceg, A., & Jackiewicz, J. 2023, *ApJ*, 954, 187, doi: [10.3847/1538-4357/acea7b](https://doi.org/10.3847/1538-4357/acea7b)
- Hill, F., Stark, P. B., Stebbins, R. T., et al. 1996, *Science*, 272, 1292, doi: [10.1126/science.272.5266.1292](https://doi.org/10.1126/science.272.5266.1292)
- Hotta, H., Bekki, Y., Gizon, L., Noraz, Q., & Rast, M. 2023, *SSRv*, 219, 77, doi: [10.1007/s11214-023-01021-6](https://doi.org/10.1007/s11214-023-01021-6)
- Hotta, H., & Kusano, K. 2021, *Nature Astronomy*, 5, 1100, doi: [10.1038/s41550-021-01459-0](https://doi.org/10.1038/s41550-021-01459-0)

- Hotta, H., Kusano, K., & Shimada, R. 2022, *ApJ*, 933, 199, doi: [10.3847/1538-4357/ac7395](https://doi.org/10.3847/1538-4357/ac7395)
- Howe, R. 2009, *Living Reviews in Solar Physics*, 6, 1, doi: [10.12942/lrsp-2009-1](https://doi.org/10.12942/lrsp-2009-1)
- Jackiewicz, J., Serebryanskiy, A., & Kholikov, S. 2015, *ApJ*, 805, 133, doi: [10.1088/0004-637X/805/2/133](https://doi.org/10.1088/0004-637X/805/2/133)
- Käpylä, P. J. 2023, *A&A*, 669, A98, doi: [10.1051/0004-6361/202244395](https://doi.org/10.1051/0004-6361/202244395)
- Karak, B. B., Käpylä, P. J., Käpylä, M. J., et al. 2015, *A&A*, 576, A26, doi: [10.1051/0004-6361/201424521](https://doi.org/10.1051/0004-6361/201424521)
- Kosovichev, A. G., & Duvall, T. L., J. 1997, in *Astrophysics and Space Science Library*, Vol. 225, SCORe'96 : Solar Convection and Oscillations and their Relationship, ed. F. P. Pijpers, J. Christensen-Dalsgaard, & C. S. Rosenthal, 241–260, doi: [10.1007/978-94-011-5167-2_26](https://doi.org/10.1007/978-94-011-5167-2_26)
- Liang, Z.-C., Birch, A. C., Duvall, Thomas L., J., Gizon, L., & Schou, J. 2017, *A&A*, 601, A46, doi: [10.1051/0004-6361/201730416](https://doi.org/10.1051/0004-6361/201730416)
- Liang, Z.-C., Gizon, L., Birch, A. C., Duvall, T. L., & Rajaguru, S. P. 2018, *A&A*, 619, A99, doi: [10.1051/0004-6361/201833673](https://doi.org/10.1051/0004-6361/201833673)
- Miesch, M. S. 2005, *Living Reviews in Solar Physics*, 2, 1, doi: [10.12942/lrsp-2005-1](https://doi.org/10.12942/lrsp-2005-1)
- Miesch, M. S., & Hindman, B. W. 2011, *ApJ*, 743, 79, doi: [10.1088/0004-637X/743/1/79](https://doi.org/10.1088/0004-637X/743/1/79)
- Nelson, N. J., Brown, B. P., Brun, A. S., Miesch, M. S., & Toomre, J. 2013, *ApJ*, 762, 73, doi: [10.1088/0004-637X/762/2/73](https://doi.org/10.1088/0004-637X/762/2/73)
- Nordlund, Å., Stein, R. F., & Asplund, M. 2009, *Living Reviews in Solar Physics*, 6, 2, doi: [10.12942/lrsp-2009-2](https://doi.org/10.12942/lrsp-2009-2)
- Parker, E. N. 1955, *ApJ*, 122, 293, doi: [10.1086/146087](https://doi.org/10.1086/146087)
- Rajaguru, S. P., & Antia, H. M. 2015, *ApJ*, 813, 114, doi: [10.1088/0004-637X/813/2/114](https://doi.org/10.1088/0004-637X/813/2/114)
- Rightmire-Upton, L., Hathaway, D. H., & Kosak, K. 2012, *ApJL*, 761, L14, doi: [10.1088/2041-8205/761/1/L14](https://doi.org/10.1088/2041-8205/761/1/L14)
- Scherrer, P. H., Bogart, R. S., Bush, R. I., et al. 1995, *SoPh*, 162, 129, doi: [10.1007/BF00733429](https://doi.org/10.1007/BF00733429)
- Schou, J., Antia, H. M., Basu, S., et al. 1998, *ApJ*, 505, 390, doi: [10.1086/306146](https://doi.org/10.1086/306146)
- Stejko, A. M., Kosovichev, A. G., & Pipin, V. V. 2021, *ApJ*, 911, 90, doi: [10.3847/1538-4357/abec70](https://doi.org/10.3847/1538-4357/abec70)
- Thompson, M. J., Toomre, J., Anderson, E. R., et al. 1996, *Science*, 272, 1300, doi: [10.1126/science.272.5266.1300](https://doi.org/10.1126/science.272.5266.1300)
- Tikhonov, A. N., & Arsenin, V. Y. 1977, New York: Winston, doi: [ISBN0-470-99124-0](https://doi.org/10.1007/978-1-4613-0000-0)
- Wang, Y. M., Nash, A. G., & Sheeley, N. R., J. 1989, *Science*, 245, 712, doi: [10.1126/science.245.4919.712](https://doi.org/10.1126/science.245.4919.712)
- Yoshimura, H. 1975, *ApJS*, 29, 467, doi: [10.1086/190355](https://doi.org/10.1086/190355)
- Zhao, J., Bogart, R. S., Kosovichev, A. G., Duvall, T. L., J., & Hartlep, T. 2013, *ApJL*, 774, L29, doi: [10.1088/2041-8205/774/2/L29](https://doi.org/10.1088/2041-8205/774/2/L29)
- Zhao, J., & Kosovichev, A. G. 2004, *ApJ*, 603, 776, doi: [10.1086/381489](https://doi.org/10.1086/381489)

APPENDIX

A. CONSTRAINTS ON THE MC PROFILE
DEvised BASED ON NUMERICAL RESULTS
FOUND IN THE RS REGIME
(THE RS-TYPE CONSTRAINT)

In this section, we present the details for how we devise the appropriate qualitative constraint for the RS regime (see also Section 5.3). We start with the constraint for the low-latitude region ($|\lambda| < 40$ degrees), in which the mass flux stream function is cylindrical (see, e.g., Figures 4 and 6 in FM15). From the theoretical perspective, such cylindrical structures that are aligned in the direction of the rotation axis are quite common in the RS regime because of the strong effects of rotation on turbulent convection.

In this study, we define the stream function Ψ so that it satisfies the following equation:

$$\rho \mathbf{U} = \nabla \times \left(\frac{\Psi}{r \sin \theta} \mathbf{e}_\phi \right), \quad (\text{A1})$$

where \mathbf{e}_ϕ is the unit vector in the azimuthal direction. Such a stream function always exists because of the mass conservation constraint. Whether the stream function Ψ is cylindrical or not can be quantitatively evaluated by looking at the derivative along the polar axis. If we define a direction parallel to the polar axis as z , the derivative along the z -axis in the polar coordinate is:

$$\frac{\partial}{\partial z} = \cos \theta \frac{\partial}{\partial r} - \frac{\sin \theta}{r} \frac{\partial}{\partial \theta}. \quad (\text{A2})$$

Combined with the definition of the stream function (A1), the z -derivative of the stream function can be expressed as:

$$\frac{\partial \Psi}{\partial z} = -\rho r \sin \theta \cos \theta U_\theta - \rho r \sin^2 \theta U_r \quad (\text{A3})$$

that shows a linear relationship between the meridional flow field and the first z -derivative of the stream function. By introducing a matrix D_{RS} , we can express the first z -derivative of the stream function as $D_{\text{RS}} \mathbf{u}$. Note that we do not consider the outermost region ($r/R_\odot > 0.965$) because the stream function may not be cylindrical in that region (Hotta in prep.). See Appendix C.4 for more details on how to compute the matrix D_{RS} .

As for the high-latitude region ($|\lambda| > 40$ degrees) where the MC profile is shaped like a single cell (ref), we have used the regularization matrix D (see Section 3.1) because it prefers a cellular structure of the MC profile. We have just modified the matrix so that the meridional

flow field in the low-latitude region ($|\lambda| < 40$ degrees), except for the outermost region as described in the last paragraph, does not contribute to regularization (more details can be found in Appendix C.2). We denote the modified regularization matrix by D' .

Finally, what we would like to minimize, in order to obtain the RLS solution with the RS-type constraint, ends up with:

$$X'_{\text{RS}} = |E^{-1/2}(\boldsymbol{\tau} - K\mathbf{u})|^2 + \alpha |D'\mathbf{u}|^2 + \boldsymbol{\kappa} \cdot C\mathbf{u} + \boldsymbol{\mu} \cdot S\mathbf{u} + \beta |D_{\text{RS}}\mathbf{u}|^2. \quad (\text{A4})$$

As shown in Section 3.2, the solution that minimizes the quantity X'_{RS} satisfies the following matrix equation:

$$\begin{pmatrix} A'' & C^T & S^T \\ C & O & O \\ S & O & O \end{pmatrix} \begin{pmatrix} \mathbf{u} \\ \boldsymbol{\kappa} \\ \boldsymbol{\mu} \end{pmatrix} = \begin{pmatrix} K^T E^{-1} \boldsymbol{\tau} \\ \mathbf{0} \\ \mathbf{0} \end{pmatrix}, \quad (\text{A5})$$

where we have introduced a $2N_j \times 2N_j$ matrix A'' that is defined as:

$$A'' = A + \beta D_{\text{RS}}^T D_{\text{RS}} \quad (\text{A6})$$

(see Equation (11) for the definition of A).

The solution thus obtained is shown in Section 5 and Appendix B.

B. EXAMPLE OF INFERRED MC PROFILES
OBTAINED WITH THE RS-TYPE
CONSTRAINT

We here show the results of MC inversion carried out with the RS-type constraint. We follow the procedures described in Section 3.3 to determine the values of the trade-off parameters and choose reasonable solutions.

We start with a trade-off plane obtained via inversion. The trade-off plane is simpler to understand compared with those in the case of the HK21 regime (Figure 2) as the residual changes monotonically against both α and β (Figure B1). This can be explained by the balance between minimization of the residual term and regularization (represented by the second and fifth terms in Equation (A4)) as we discussed in Section 4. Such a simple trade-off plane may be related to the fact that we have imposed two kinds of regularization independently for low- and high-latitude regions (see Appendix A), i.e., minimization of the regularization term $\alpha |D'\hat{\mathbf{u}}_{\text{cand}}|^2$ does not conflict with minimization of the other regularization term $\beta |D_{\text{FM}}\hat{\mathbf{u}}_{\text{cand}}|^2$.

We then present an example of inferred MC profiles that is obtained with the trade-off parameters $(\alpha, \beta) =$

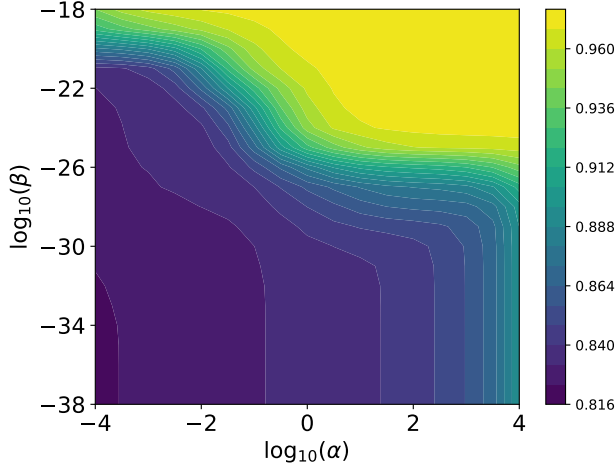


Figure B1. Trade-off plane in the case of MC inversion with the RS-type constraint. The values of the residual term are shown as a function of the trade-off parameters α and β . Brighter colors represent larger residual terms. The figure shows a trade-off relation between the residual term and regularization terms, namely, that the residual term becomes larger with the increasing trade-off parameters.

($10^{-1.6}, 10^{-14.5}$). Figure B2 shows the radial and latitudinal components of the inferred meridional flow field (U_r and U_θ). The subsurface MC is characterized by a poleward flow as shown in Section 4, and the poleward flow is fairly thin, and the amplitude of U_θ is small ($< 3 \text{ m s}^{-1}$) in most of the convective zone ($r/R_\odot < 0.9$). The radial component U_r also exhibits a relatively small velocity amplitude $< 0.5 \text{ m s}^{-1}$ inside the low-latitude convective zone compared with those of the single- or double-cell MC profiles (see Figures 3 and 5). Such an MC profile is required for realizing a mass flux stream function with a cylindrical profile in the low-latitude region ($\lambda < 40$ degrees) and a single-cell profile in the high-latitude region ($\lambda > 40$ degrees) (see Figure 11 in the main text) that is similar to the results found in the RS regime (see, e.g., Figure 6c in FM15).

When we take a look at slices of U_θ (Figure B3), the difference between the meridional flow field in the low-latitude region and that in the high-latitude region is rather obvious. While the poleward flow is confined in a narrow layer ($r/R_\odot < 0.95$) in the low-latitude region, it becomes broader in the high-latitude region, reaching the depth of $r/R_\odot \sim 0.88$ at $\lambda = 45$ degrees. We also find an equatorward flow below the thick poleward flow (see around $0.8 < r/R_\odot < 0.9$ of the upper-right panel in Figure B3). The thicker and faster flows in the high-latitude region lead to much more mass flux compared with that in the low-latitude region (left in Figure B4).

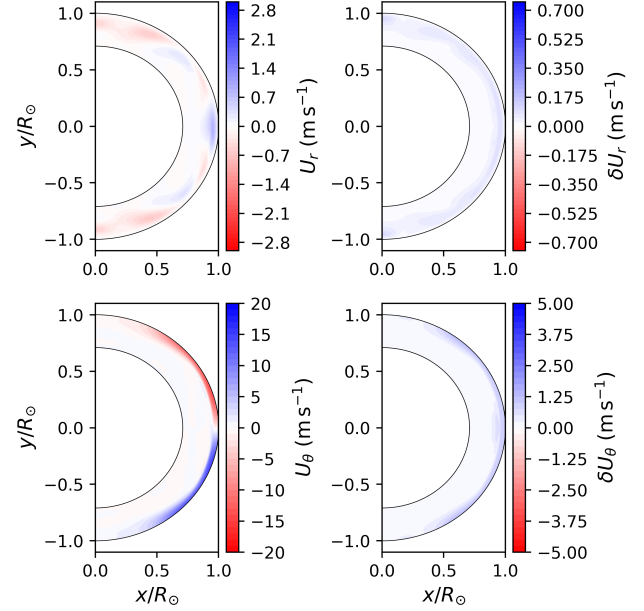


Figure B2. Radial and latitudinal components of the meridional flow field inferred via inversion with the RS-type constraint (upper-left and lower-left, respectively). The corresponding uncertainties are shown in the right panels. The trade-off parameters $\alpha = 10^{-1.6}$ and $\beta = 10^{-14.5}$ are used. The results show that the meridional flow velocity is almost zero well inside the convective zone ($r/R_\odot < 0.9$).

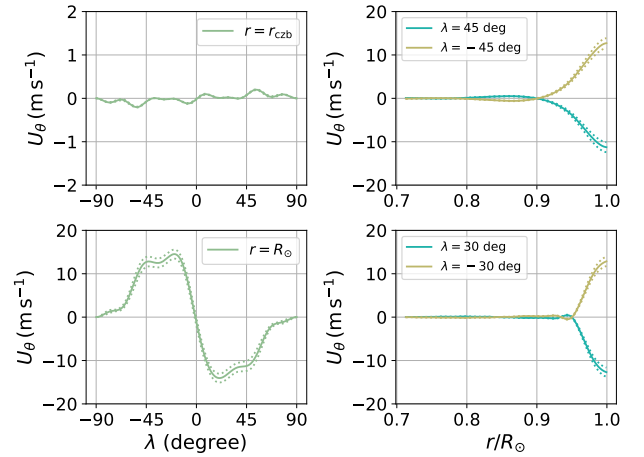


Figure B3. Slices of the latitudinal component of the inferred cylindrical MC profile. The left panels show the slices at certain radii, namely, $r = r_{czb}$ (upper) and $r = R_\odot$ (lower), and the right panels show those at certain latitudes, namely, $|\lambda| = 45$ degrees (upper) and $|\lambda| = 30$ degrees (lower). In the right panels, turquoise (sandy yellow) represents the northern (southern) hemisphere.

Interestingly, the AM fluxes in both latitudes are compa-

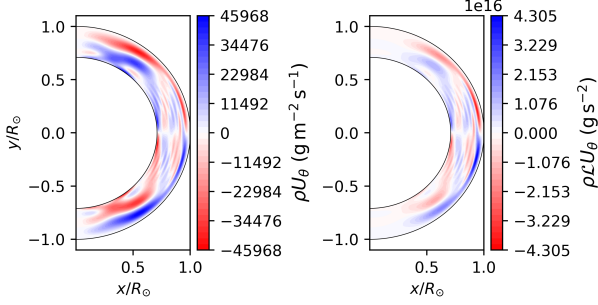


Figure B4. Mass flux ρU_θ (left) and AM flux $\rho \mathcal{L} U_\theta$ (right) computed with the MC profile shown in Figure B2. The low-latitude region ($|\lambda| < 40$ degrees) is characterized by the cylindrical profile in both mass and AM fluxes.

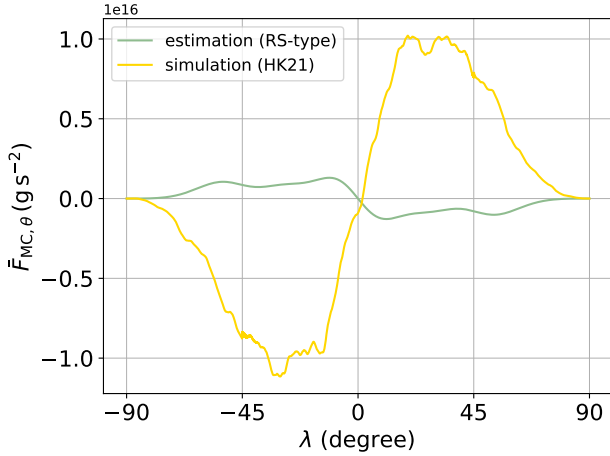


Figure B5. Latitudinal AM fluxes by MC that are radially averaged $\bar{F}_{MC,\theta}(\theta)$ (Equation (C22)) as a function of the latitude. The averaged AM flux computed with the result of HK21 (yellow) indicates the equatorward AM transport while that computed with the inferred cylindrical MC profile (green) indicates the poleward AM transport. It is also seen that AM flux by MC in the case of the cylindrical profile contributes less to the total MC transport compared with that of the numerical simulation.

rable to each other (right in Figure B4). This is because of the factor $\sin \theta$ in \mathcal{L} , canceling the contrast seen in the mass flux between the high- and low-latitude regions. It is also noteworthy to mention that the magnitude of the AM flux ($\sim 10^{16} \text{ g s}^{-2}$) is smaller than those of the single- or double-cell MC profiles ($\sim 10^{17-18} \text{ g s}^{-2}$) (see Figure 8), highlighting the lower contribution to the net AM flux by MC in the case of the MC profile inferred with the RS-type constraint (Figure B5).

C. NOTES ON THE REGULARIZATION MATRICES

Details on how we have computed the regularization matrices are presented in this section. After we show a linear relation between the meridional flow field \mathbf{U} and the expansion coefficient \mathbf{u} in Appendix C.1, specific procedures to compute the regularization matrices, namely, D (Appendix C.2), D_{HK1} and D_{HK2} (Appendix C.3), and D_{RS} (Appendix C.4) are given.

C.1. A linear relation between \mathbf{u} and \mathbf{U}

As shown in the main text, regularization has been imposed on the meridional flow field \mathbf{U} , but the corresponding regularization terms are expressed in terms of the expansion coefficient \mathbf{u} . We thus show a relation between \mathbf{U} and \mathbf{u} in this section.

We first introduce a $2N_D$ -dimensional vector \mathbf{U}_{1d} in which N_D is the product of the number of mesh points in the radial direction N_r and that in the latitudinal direction N_θ . In the case of the data provided by G20, N_r and N_θ are 178 and 181, respectively. The first N_D components in \mathbf{U}_{1d} correspond to $U_r(r, \theta)$ in the following way:

$$(\mathbf{U}_{1d})_{j'} = U_r(r_{k'}, \theta_{l'}), \quad (\text{C7})$$

where k' runs from 1 to N_r , l' runs from 1 to N_θ , and $j' = N_\theta \times (k' - 1) + l'$. Similarly, the latter N_D components in \mathbf{U}_{1d} correspond to $U_\theta(r, \theta)$ as follows:

$$(\mathbf{U}_{1d})_{N_D+j'} = U_\theta(r_{k'}, \theta_{l'}), \quad (\text{C8})$$

with the same indices used in Equation (C7).

Let us denote the N_D -dimensional vectors (C7) and (C8) by $\mathbf{U}_{1d,r}$ and $\mathbf{U}_{1d,\theta}$, and then Equation (2) can be rewritten as

$$(\mathbf{U}_{1d,s})_{j'} = \sum_j u_{s,j} Q_k(r_{k'}) P_l(\cos \theta_{l'}), \quad (\text{C9})$$

where k runs from 1 to N_k , l runs from 1 to N_l , $j = N_l \times (k - 1) + l$, and $s = r$ or θ (see also Section 2). By introducing a $2N_D \times 2N_j$ matrix G , we have a linear relation between \mathbf{U}_{1d} and \mathbf{u} :

$$\mathbf{U}_{1d} = G\mathbf{u}, \quad (\text{C10})$$

where G consists of an $N_D \times N_j$ matrix G' with which

$$G = \begin{pmatrix} G' & O \\ O & G' \end{pmatrix}. \quad (\text{C11})$$

Elements in the matrix G' are given as

$$(G')_{j'j} = Q_k(r_{k'}) P_l(\cos \theta_{l'}). \quad (\text{C12})$$

C.2. How to compute the regularization matrix D

Following G20, we consider the weighted vorticity of the meridional flow field that is defined as $[\partial_r(rU_\theta) - 10\partial_\theta U_r]/r$ where ∂_s stands for the partial derivative in terms of the variable s . We define an $(N_r - 1)(N_\theta - 1) \times 2N_D$ matrix D_v so that the norm $|D_v \mathbf{U}_{1d}|^2$ represents the surface integral of the squared weighted vorticity over the whole meridional plane at a certain azimuth. In this paper, the forward difference and trapezoidal integration have been adopted, and elements of D_v are given in the following way:

$$(D_v)_{j'_0 j'_1} = (D_v)_{j'_0(j'_2)} = 10 \sqrt{\frac{\Delta r_{k'}}{4(r_{k'+1/2})\Delta\theta_{l'}}}, \quad (\text{C13})$$

$$(D_v)_{j'_0(j'_1+1)} = (D_v)_{j'_0(j'_2+1)} = -10 \sqrt{\frac{\Delta r_{k'}}{4(r_{k'+1/2})\Delta\theta_{l'}}}, \quad (\text{C14})$$

$$(D_v)_{j'_0 j'_3} = (D_v)_{j'_0(j'_3+1)} = -r_{k'} \sqrt{\frac{\Delta\theta_{l'}}{4(r_{k'+1/2})\Delta r_{k'}}}, \quad (\text{C15})$$

and

$$(D_v)_{j'_0 j'_4} = (D_v)_{j'_0(j'_4+1)} = r_{k'+1} \sqrt{\frac{\Delta\theta_{l'}}{4(r_{k'+1/2})\Delta r_{k'}}}, \quad (\text{C16})$$

where $\Delta r_{k'} = r_{k'+1} - r_{k'}$, $\Delta\theta_{l'} = \theta_{l'+1} - \theta_{l'}$, and $r_{k'+1/2} = (r_{k'} + r_{k'+1})/2$. The indices are defined as below:

$$j'_0 = (N_\theta - 1) \times (k' - 1) + l', \quad (\text{C17})$$

$$j'_1 = N_\theta \times (k' - 1) + l', \quad (\text{C18})$$

$$j'_2 = j'_1 + N_\theta, \quad (\text{C19})$$

$$j'_3 = j'_1 + N_D, \quad (\text{C20})$$

and

$$j'_4 = j'_2 + N_D. \quad (\text{C21})$$

Note that k' runs from n_{czb} to $n_{\text{surf}} - 2$ with which $r_{n_{\text{czb}}} = r_{\text{czb}}$ and $r_{n_{\text{surf}}} = R_\odot$, respectively. The index l' runs from 1 to $N_\theta - 1$. The elements other than the ones designated above are zero. With the linearity between \mathbf{U}_{1d} and \mathbf{u} (Equation (C10)), the regularization matrix D can be expressed as $D = D_v G$.

As for the modified regularization matrix D' that is used in the RS-type constraint (see Section 5.3), we prepare an $(N_r - 1)(N_\theta - 1) \times 2N_D$ matrix D'_v whose j'_0 -th row is identical to that of D_v when a point $(r_{k'}, \theta_{l'})$ satisfies either a condition $r_{k'}/R_\odot > 0.965$ or another condition $r_{k'}/R_\odot < 0.965$ and $|\pi/2 - \theta_{l'}| > \pi/9$ with $j'_0 = N_\theta \times (k' - 1) + l'$. The ranges of the indices are the same as those when we compute D_v . For the other (p, q) elements, $(D'_v)_{pq} = 0$. The matrix D' is then given as $D' = D'_v G$.

C.3. How to compute the regularization matrices D_{HK1} and D_{HK2}

In order to compute the regularization matrices D_{HK1} and D_{HK2} used in MC inversion with the HK21-type constraint, we first consider an $N_\theta \times 2N_D$ matrix D_{HK} with which $D_{\text{HK}} \mathbf{U}_{1d}$ represents the latitudinal AM flux by MC that is radially averaged, namely,

$$\bar{F}_{\text{MC},\theta}(\theta) = \frac{\int_0^{2\pi} \int_{r_{\text{czb}}}^{R_\odot} F_{\text{MC},\theta}(r, \theta) r \sin\theta dr d\phi}{\int_0^{2\pi} \int_{r_{\text{czb}}}^{R_\odot} r \sin\theta dr d\phi}. \quad (\text{C22})$$

We consider the trapezoidal integration over the radius, and elements in the matrix D_{HK} are given as below:

$$(D_{\text{HK}})_{l' j'_3} = \rho_{k'} \mathcal{L}_{k',l'} \times \frac{2r_{k'}(\Delta r_{k'-1/2})}{(R_\odot^2 - r_{\text{czb}}^2)} \quad (\text{C23})$$

for $k' = n_{\text{czb}} + 1$ to $n_{\text{surf}} - 2$,

$$(D_{\text{HK}})_{l' j'_3} = \rho_{k'} \mathcal{L}_{k',l'} \times \frac{r_{k'} \Delta r_{k'}}{(R_\odot^2 - r_{\text{czb}}^2)} \quad (\text{C24})$$

for $k' = n_{\text{czb}}$, and

$$(D_{\text{HK}})_{l' j'_3} = \rho_{k'} \mathcal{L}_{k',l'} \times \frac{r_{k'} \Delta r_{k'-1}}{(R_\odot^2 - r_{\text{czb}}^2)} \quad (\text{C25})$$

for $k' = n_{\text{surf}} - 1$. Note that l' runs from 1 to N_θ . The index j'_3 is defined by Equation (C20). The mean $\Delta r_{k'-1/2}$ is defined as $\Delta r_{k'-1/2} = (\Delta r_{k'-1} + \Delta r_{k'})/2$. The density at $r = r_{k'}$ is denoted by $\rho_{k'}$ whose value is determined by the standard solar model (Christensen-Dalsgaard et al. 1996). The specific AM is $\mathcal{L}_{k',l'} = (r_{k'} \sin\theta_{l'})^2 \Omega_{k',l'}$, and the averaged angular velocity ($\sim 2\pi \times 413$ nHz) is used for $\Omega_{k',l'}$. The regularization matrix D_{HK1} represents the latitudinal average of $\bar{F}_{\text{MC},\theta}(\theta)$ in each hemisphere. We therefore define two matrices for the latitudinal averaging. One is an $(N_\theta - 1) \times N_\theta$ matrix D_{m} defined as follows:

$$(D_{\text{m}})_{l'l} = (D_{\text{m}})_{l'(l'+1)} = \frac{1}{2} \quad (\text{C26})$$

where l' runs from 1 to $N_\theta - 1$. The other one is a $2 \times (N_\theta - 1)$ matrix D_{int} whose elements are

$$(D_{\text{int}})_{1l'} = \frac{\Delta\theta_{l'}}{\pi/2} \quad (\text{C27})$$

for $l' = 1$ to $N_\theta/2$, and

$$(D_{\text{int}})_{2l'} = \frac{\Delta\theta_{l'}}{\pi/2} \quad (\text{C28})$$

for $l' = N_\theta/2 + 1$ to $N_\theta - 1$. Using the two matrices D_{m} and D_{int} in addition to the linear relation (C10), the regularization matrix D_{HK1} can be expressed as $D_{\text{HK1}} = D_{\text{int}} D_{\text{m}} D_{\text{HK}} G$.

The other regularization matrix D_{HK2} represents the first derivative of $\bar{F}_{\text{MC},\theta}(\theta)$ in terms of the colatitude. We have introduced an $(N_\theta - 1) \times N_\theta$ matrix D_θ with which the norm $|D_\theta \mathbf{U}_{1d}|^2$ is the integration of $|\partial_\theta \bar{F}_{\text{MC},\theta}|^2$ over the colatitude. Based on the trapezoidal integration scheme, elements in the matrix D_θ are given as

$$(D_\theta)_{l'l'} = -(D_\theta)_{l'(l'+1)} = -\frac{\cos^6(\theta_{l'+1/2}) + 0.15}{\sqrt{\Delta\theta_{l'}}}, \quad (\text{C29})$$

where l' runs from 1 to $N_\theta - 1$. The mean colatitude $\theta_{l'+1/2} = (\theta_{l'} + \theta_{l'+1})/2$ has been introduced. We have an extra term in the numerator in addition to the ordinary trapezoidal integration scheme, which is considered to suppress the rapidly varying $\bar{F}_{\text{MC},\theta}(\theta)$ in the high-latitude region. We can then express D_{HK2} as follows: $D_{\text{HK2}} = D_\theta D_{\text{HK}} G$.

C.4. How to compute the regularization matrix D_{RS}

As described in Appendix A, the RS-type constraint is represented by using the two regularization matrices D' and D_{RS} . We have already given how to compute D' in Appendix C.2, and we focus on D_{RS} in this section. The starting point is the linear relation between the first z -derivative of the mass flux stream function and the meridional flow field (see Equation (A3)). The z -derivative of the stream function can then be expressed in a vector form as $D_z \mathbf{U}_{1d}$ where an $N_D \times 2N_D$ matrix D_z is defined as follows:

$$(D_z)_{j'_1 j'_1} = -\rho_{k'} r_{k'} \sin^2 \theta_{l'}, \quad (\text{C30})$$

and

$$(D_z)_{j'_1 j'_3} = -\rho_{k'} r_{k'} \sin \theta_{l'} \cos \theta_{l'}, \quad (\text{C31})$$

where k' runs from 1 to N_r and l' runs from 1 to N_θ . The indices j'_1 and j'_3 are defined by Equations (C18) and (C20). Because the mass flux stream function is cylindrical only in the low-latitude region (see, e.g., Figure 6c in FM15), we set an entry in D_z to be zero unless the corresponding point $(r_{k'}, \theta_{l'})$ falls into a region defined by a condition that $r/R_\odot < 0.965$ and $|\pi/2 - \theta_{l'}| < \pi/9$. We eventually obtain an expression for the matrix D_{RS} : $D_{\text{RS}} = D_z G$.